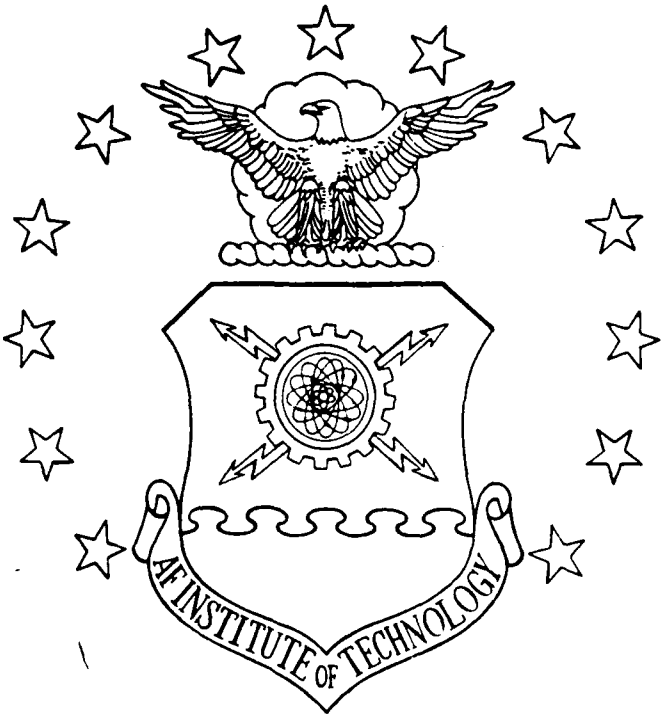

A PRELIMINARY STUDY ON THE USE OF THE ULTRAVIOLET EXHAUST PLUMES OF ICBMS FOR LAUNCH DETECTION

THESIS

Stuart D. Williams
Captain, USAF

AFIT/GSO/ENP/86D-3

DEPARTMENT OF THE AIR FORCE
AIR UNIVERSITY
AIR FORCE INSTITUTE OF TECHNOLOGY

Wright-Patterson Air Force Base, Ohio

AFIT/GSO/ENP/86D-3

A PRELIMINARY STUDY ON THE USE OF THE ULTRAVIOLET EXHAUST PLUMES OF ICBMS FOR LAUNCH DETECTION

THESIS

Stuart D. Williams
Captain, USAF

AFIT/GSO/ENP/86D-3

AFIT/GSO/ENP/86D-3

A PRELIMINARY STUDY ON THE USE OF THE ULTRAVIOLET EXHAUST PLUMES OF ICBMS FOR LAUNCH DETECTION

THESIS

Presented to the Faculty of the School of Engineering
of the Air Force Institute of Technology
Air University
In Partial Fulfillment of the
Requirements of the Degree of
Master of Science in Space Operations

Stuart D. Williams, B.S.
Captain, USAF

November 1986

PREFACE

This thesis is concerned with investigating the possibilities of exploiting the ultraviolet plumes of ICBMs for launch detection. The motivation for selecting this topic stemmed from the renewed interest in the remote sensing community on this subject brought on primary by the Strategic Defense Initiative. The goal of this thesis was to present a first cut analysis into the UV launch detection problem and to provide a starting point for further study should it be warranted.

There are many individuals who have helped and encouraged me throughout the ordeal of this thesis. Among those many, I would especially like to thank my advisor, Maj Jim Lange, for his guidance, patience and unfailing willingness to help regardless of his personal workload. Also, a note of thanks to the staff of the AFIT Library who's help was invaluable during the research of this topic.

Finally, a special thanks to my wife Julie whose encouragement and never tiring help made the completion of this work possible.

Stuart D. Williams

Table of Contents

List of Figures

List of Tables

Abstract

The purpose of this investigation was to conduct preliminary research into the use of the ultraviolet plumes of ICBMs for launch detection. The thrust of this research was in an effort to exploit the middle UV (200-300 nm) for launch detection and possible tracking. Specifically, this thesis reviewed the current open literature on the UV signatures of ICBMs, current ultraviolet background data, the state of UV detector technology, and simple sensor design considerations. From these investigations a baseline sensor system was assumed which was compatible with existing technology.

Using the baseline sensor system, representative target intensities and background radiances, first order signal-to-noise calculations were performed. The results of these calculations revealed that the current state of UV detector technology and the magnitude of representative plume intensities are sufficient to allow for ICBM detection from a geosynchronous sensor system. However, because of the UV target signal absorption by the ozone layer, adequate SNR can not be maintained below approximately 40-50 km. These results indicate that further study into this problem is warranted and several recommendations are included for consideration.

A PRELIMINARY STUDY ON THE USE OF THE ULTRAVIOLET EXHAUST PLUMES OF ICBMS FOR LAUNCH DETECTION

I. Introduction

During the 1960's through the early 1970's, much research was conducted on the feasibility of using the ultraviolet (UV) spectrum for ballistic missile launch detection. Many programs were initiated to measure UV emissions (Jacobs, Gay, Dorian), and the focus of this work centered on compiling accurate measurements of UV plume emissions. Most of these early programs were conducted from ground based or airborne sensors which monitored launches from Cape Canaveral. The early interest during this period was the possibility of exploiting portions of the middle UV region from about 200-300 nanometers and later the vacuum UV region from about 100-200 nanometers. In this region there was little UV background radiance contributed by the earth, and signal detection seemed promising. "However, interest waned after several years of inconclusive study on whether signals would be 'brighter' than the earth" (McGregor, 1985:3). The issue was further clouded by the characteristic non-thermal behavior of UV emissions which eluded easy comprehension and modeling (Daugherty, 1986:5). Because of these issues, the practicality of UV launch

detection was questioned, and interest dwindled in favor of the much brighter and easily modeled infrared (IR) plume signature.

In 1983, the commitment of President Reagan and this country to the Strategic Defense Initiative renewed interest in the exploitation of UV missile signatures for launch detection. Several developments have helped stimulate this interest. One such development is the availability of better UV background data collected primarily by the Orbiting Geophysical Observatory satellites (McGregor, 1985:3). Another key development has been the improving UV sensor technology, especially the development of higher UV sensitive photocathodes, charged coupled devices (CCD) and high gain microchannel plates. For these reasons interest is again focused on the middle UV as a possible candidate for launch detection.

The use of the middle UV for launch detection offers several advantages over the current IR detection systems. The first and most promising advantage is the belief that the UV plume of an ICBM is much smaller in size than its IR plume and that it appears only very close to the rocket nozzle. This might help fulfill the detection and tracking requirements of SDI which dictate accurate ICBM location data. Other key advantages include the possibility of using the earth's UV airglow as a uniform background in which rising ICBMs UV signatures could be detected and tracked

with the low possibility of false alarms due to intense UV sources, and the virtual impossibility of blinding the sensor by using a ground based laser system.

Statement of the Problem

The purpose of this research is to review the current knowledge on the UV signatures of ICBMs, UV background data, and state of UV sensor technology, and to accomplish first order signal-to-noise calculations to determine if UV signal detection is possible from a space platform.

Sequence of Presentation

This thesis is organized as follows: Chapter I contains the introduction; Chapter II presents the methodology used; Chapter III reviews the target characteristics; Chapter IV investigates the atmospheric transmission processes; Chapter V reviews the background radiation; Chapter VI analyzes sensor requirements; Chapter VII presents the results; and Chapter VIII contains conclusions and recommendations.

II. Methodology

The proposed investigation of this thesis is essentially an application of the classic elements of the remote sensing problem to the UV spectrum. These elements can be classified as the sources, atmospheric and background effects, and the sensors. Specifically, these elements are the exhaust plume of the ICBM as the target source; the UV background of the earth as the background source; the transmission of the target signal through the upper atmosphere to the space borne sensor; and, finally, the state of the current UV detector technology as the sensor element. In order to compare alternative systems, it is desired to combine all these factors into a single figure-of-merit for comparison.

Signal-to-Noise Ratio

The most useful figure-of-merit for a remote sensing system is the concept of signal-to-noise ratio. In the application of any remote sensor, the goal of the system is to detect the desired signal over any unwanted or background signal. The ability of the system to accomplish this goal can be measured by the use of the signal-to-noise ratio. Basically, the signal-to-noise ratio is a confidence measure of detecting the target current against the unwanted noise current.

Generally, it is desired that the signal-to-noise ratio (SNR) be as large as possible to achieve a high degree of confidence in the detection of a target signal. Signal-to-noise ratios of at least five are desirable.

The signal-to-noise ratio for a shot-noise limited photocathode UV sensor (Kingston, 1979:13-16) operating in pulse counting mode is as follows:

$$S/N = \frac{\left(I_T/e\right)\left(T_d\right)^{1/2}}{\left(I_B/e + I_T/e\right)^{1/2}}$$

where

I_T - target current

I_B - background current

T_d - integration time

e - 1.6×10^{-19} coulombs

Current Calculations

The calculations of the target and background currents come from basic radiometric equations.

$$I_T = \frac{e\, A_r}{h\, c\, r^2} \int_{\lambda_1}^{\lambda_2} I_\lambda \tau_o \tau_a G \eta \lambda \, d\lambda$$

$$I_B = \frac{e\, A_r \Omega_r}{hc} \int_{\lambda_1}^{\lambda_2} L_\lambda \tau_o \tau_a G \eta \lambda \, d\lambda$$

where

A_r - area of receiver optics

Ω_r - solid angle of receiver

I_λ - spectral intensity (watts/ster-μm)

L_λ - spectral radiance (watts/ster-m^2-μm)

γ_o - optic transmission

γ_a - atmospheric transmission

G - gain

η - quantum efficiency

λ - wavelength

r - range

e - 1.602×10^{-19} coulombs

h - 6.626×10^{-34} joule-sec

c - 2.997×10^{8} meters/sec

The approach will be to investigate each of the remote sensing elements (sources, atmospheric and background effects, and sensors) to determine the appropriate input values for the radiometric equations. This will be achieved by addressing the following four objectives.

First, the target source will be investigated. This will include an analysis of the threat scenario, the UV emission mechanisms, and the magnitude of the UV signature. Once this analysis has been made, the second objective will be to consider what amount of UV radiation is actually received by the collecting optics on the space platform.

This will involve the consideration of the exhaust plume transmission through the atmosphere. The third objective is to evaluate the amount of background UV radiation emitting from the primary background source--the earth's atmosphere. Finally, the last objective will be to investigate the current technology of UV imaging detectors and their application to the proposed sensor platform.

Once these four objectives are achieved, a signal-to-noise calculation will be made based on the spectral signature of the target source and the spectral bandpass of the chosen sensor system. From these calculations it will be possible to ascertain if the target signal can be distinguished from the background signal and, hence, detected.

III. Target Characteristics

Threat

The first problem is to analyze the threat and develop a general scenario for evaluating the proposed sensor system. This is to be accomplished by addressing four issues. First, a generic ballistic missile trajectory will be developed to determine times of powered flight and maximum altitudes. Second, a brief survey of propulsion systems will be accomplished to review the possible types of propellants in use. This is important since propellant types and their combustion processes probably affect the UV emission. Third, candidate UV mechanisms will be reviewed, and finally, generalized emission data will be developed for threat ballistic missiles.

TABLE I

Current Soviet ICBMs.
(Soviet Military Power, 1986)

System	Propellant	Number Deployed
SS-11	Liquid	448
SS-13	Solid	60
SS-17	Liquid	150
SS-18	Liquid	308
SS-19	Liquid	360
SS-25	Solid	70+
SS-Ns	Most all are Liquid	983

Table I lists the currently deployed Soviet ICBM systems, the type of propellant used and the approximate number of systems deployed.

Ballistic Missile Trajectories

For purposes of this thesis, it is necessary to develop a generic ICBM trajectory with emphasis on the boost phase. The goal is to develop a generic duration of boost as well as altitude of burnout. Both are important in the context of launch detection and tracking.

From a ballistic missile defense perspective, it is highly desirable to detect and begin initial target tracking as soon after launch as possible. This is driven by the desire to kill the ICBM target during the boost phase prior to MIRV deployment. Second, and more important to this thesis, is the fact that during the boost phase the UV signature will be at its brightest and therefore will afford the best opportunity for detection. During the high thrust boost phase the UV plume is brightest, while the UV plume from a low thrust maneuvering RV bus engine is much dimmer.

In order to get a feel for the times and altitudes involved, it is important to distinguish between the slow burn and the fast burn ICBMs. This is probably the most important variation that occurs during the boost phase. Slow burn ICBMs are generally of the liquid fuel type, slow to accelerate, and burn out at relatively high altitudes.

In comparison, solid propellants are faster to accelerate and can be manufactured with very fast burntimes, resulting in much lower burnout altitudes (Carter, 1984:8).

For example, the Soviet SS-18 ICBM, which is liquid-fueled and the largest Soviet ICBM, has a burnout time on the order of five minutes and burnout altitude of 300-400 km. By comparison, the US Peacekeeper has a burnout time and altitude of three minutes and 200 km, respectively (Carter, 1984:10). A comparison of several ICBM systems is shown in Table II.

TABLE II

ICBM Burnout Times and Altitudes.
(Carter, 1984:10)

System	Propellant	Burnout Time	Burnout Altitude
SS-18	Liquid	300 sec	400 km
Peacekeeper	Solid	180 sec	200 km
Midgetman (fast burn)	Solid	50 sec	80 km
Midgetman (low flight profile)	Solid	220 sec	100 km

Several conclusions can be drawn from the data in Table II. In light of the fact that most Soviet systems are liquid fueled, and the solid systems replacing these systems are not of the fast burn variety (Soviet Military Power, 1986:24-28), Soviet systems can be expected to have burnout

times on the order of one to five minutes with most systems favoring the latter.

Furthermore, for the near future the lowest altitude of burnout will probably be about 80-100 km. Although it is technically feasible to build fast burn ICBMs, such as the proposed fast burn Midgetman, the deployment of these systems is uncertain. These fast burn systems with low burnout altitudes enhance survivability but reduce the maximum throw weight and RV accuracy. According to a Martin Marietta study cited by Carter, for a burnout altitude below about 90 km the atmosphere becomes too dense for accurate RV deployment (Carter, 1984:8).

In summary, the lowest possible burnout we can expect from Soviet ICBMs in the near future is about 90-100 km with an upper bound at about 300-400 km. If the Soviets build and deploy a fast burn ICBM, then burnout altitudes as low as 80km might be expected depending on the desired RV accuracy. Additionally, burn times should range from about one to five minutes respectively with currently deployed systems.

Propulsion Systems

The propulsion system of an ICBM is important to the detection of the UV emission spectrum of the plume for several reasons. First, as previously discussed, the type of system, either slow or fast burn, will determine the amount of time the plume will be visible as well as the

altitude at which burnout occurs. Second, the chemical composition of the propellants will help determine what possible UV mechanisms are responsible for the UV signature.

Propulsion systems are usually classified by the types of fuels that are used, solid or liquid, and can be further divided by their chemical composition. The liquid fuel systems are virtually all slow burn with slow acceleration, long burn times, and fairly high burnout at altitudes. In contrast, solid fuels are generally faster burning and have the capability for shorter burn times and, subsequently, lower burnout altitudes. According to the DOD report Soviet Military Power, the majority of currently deployed Soviet ICBMs and SLBMs are liquid fueled (See Table I). Therefore we can expect most Soviet ICBMs to have long burntimes and fairly high burnout altitudes.

Although the majority of current Soviet ICBMs are liquid fueled, Soviet trends indicate a shift from liquid to solid fueled ICBMs and SLBMs (Soviet Military Power, 1986). Therefore, in the future we can expect that Soviet ICBMs will be moving toward the faster burning solid ICBMs with substantially shorter burn times and lower burnout altitudes.

Liquid Fuels. From a generic standpoint, all liquid fuel ICBMs use an oxidizer and a fuel. The combination of these and their subsequent combustion causes the UV

signature to develop. Table III shows some of the common liquid fuels and oxidizers in use today.

TABLE III

Fuels and Oxidizers.
(Sutton and Ross, 1976:233-257)

Oxidizers	Fuels
Liquid Oxygen (O_2)	Hydrocarbons (Kerosene, JP-4)
Liquid Fluorine (F_2)	Hydrazine (N_2H_4)
Hydrogen Peroxide (H_2O_2)	Liquid Hydrogen (H_2)
Nitric Acid (HNO_3)	Liquid Ammonia (NH_3)
Nitrogen Tetroxide (N_2O_4)	Ethyl Alcohol (C_3H_5OH)
Chlorine Trifluoride (ClF_3)	Unsymmetrical Dimethylhydrazine (UDMH) (CH_3NNH_2)

In the past, many of the larger liquid fueled boosters tended to use the liquid oxygen and hydrocarbons as propellants because of their relatively low cost and easy handling characteristics. US systems such as Atlas, Thor, Jupiter, and Titan I all employed these propellants. The Titan II ICBM system uses a storable liquid fuel consisting of UDMH and nitrogen tetroxide (Davies, 1985:36) which is not unlike the Soviet Proton satellite launch vehicle propellant which has been in service since 1965 (Pauw, 1986:250).

When a fuel and oxidizer are mixed together and burned many chemical reactions can take place. For example, those propellants which involve any hydrocarbons tend to yield various amounts of CO, H_2O, H_2, CO_2, OH, H, and O_2. Additionally, those propellants which use a nitrogen based fuel also tend to yield, in addition to the above, N_2 and NO. As will be seen, these chemical reactions probably are in part responsible for the UV plume.

From the threat perspective, Soviet development of liquid fuel systems has been similar to that of the US. Early Soviet systems tended to use hydrocarbon and liquid oxygen propellants. Although current Soviet ICBM fuels are difficult to assess, several large plants for manufacturing UDMH have been built, and it is speculated that newer ICBMs may be using UDMH in combination with nitrogen tetroxide as propellants (Bonds, 1976:219). Additionally, as mentioned above there are several current Soviet launch vehicles employing these propellants (Pauw, 1986:250). Furthermore, in view of the Soviet philosophy of sticking with proven systems, it seems unlikely that the Soviets have developed any type of "exotic" propellant system. Therefore, it seems logical to assume that Soviet liquid fuel ICBM systems are not wholly unlike similar US systems, especially the Titan II.

Solid Propellants. From the standpoint of ICBMs, solid propellants are more practical than liquid propellants

because of their relatively safe handling characteristics and easy storability. As a result, all US ICBMs are solid fueled, and as previously stated the Soviet's trend is to replace current liquid fuel systems with solid fueled systems.

Solid propellants are generally composed of fuels, oxidizers, binders, curing agents, and burn rate catalysts (Sutton and Ross, 1976:395). Because of the wide variety of solid propellants, it would be impossible to list all of the possible combinations of these components. However, the most common solid fuel and oxidizer are aluminum powder and ammonium perchlorate (NH_4ClO_4) (Sutton and Ross, 1976:395). Interestingly enough, the use of aluminum powder is thought to be significant from a UV signature perspective. It is is believed that the high temperature Al_2O_3 particles in the exhaust constituents play a key role in the UV emission.

From the threat context, little is published in the open literature about the actual composition of Soviet solid propellants. It is known that Soviet solid propellants did not evolve as quickly as US propellants, but the gap is closing fast. Again it seems unlikely that the Soviet solid systems would be radically different from US systems. Furthermore, since aluminum powder is an excellent fuel and is relatively abundant and inexpensive, it seems plausible that it plays a key role in the Soviet's solid systems.

Target Radiation Mechanisms

The source of UV emissions from an ICBM can be divided into three groups: 1) the emissions from the chemicals in the plume of the exhaust, 2) chemical reactions of combustion products with surrounding atmosphere, and 3) scattered sunlight off gases in the plume (McIntyre and others, 1981,3-2).

In both liquid and solid fueled ICBMs, it is some composition of these process that creates IR and UV plumes. As mentioned before, the IR plume is now more easily understood and modeled, whereas this task is not so easily accomplished with the UV plume. There are, however, several candidate mechanisms for the creation of an UV plume signature. These include the following:

1. Thermal Emission
2. Chemiluminescence
3. Searchlight Emission
4. Hot Particles Suffering Thermal Lag
5. Particle Emissions
6. Molecular Electronic Emissions
   (Slack and others, 1983,18)

All of these emission mechanisms are manifestations of the ICBM's exhaust plume or, more specifically, the combustion process of the fuel and/or its interaction with the surrounding atmosphere. Although each of the listed mechanisms is expected to contribute to the UV plume signature, the analysis of the relative contribution of each mechanism gives ambiguous results. "The major expected contributors to UV radiation, particle thermal emission and

CO + O chemiluminescence, combine to yield a featureless continuum on which the relative contributors cannot be easily determined from observed spectra" (Wormhoudt and Lyons, 1981,2-15). Since particle thermal emissions and chemiluminescence are the most likely candidates, they will be discussed in detail in the following pages.

Thermal Emissions. The thermal blackbody emission process occurs because of a body's temperature. All objects radiate at wavelengths and power levels determined primarily by their temperature. As the temperature of a body is increased, the amount of radiation given off increases and the wavelength of maximum emission becomes shorter. As expected, the temperature in the exhaust plume of an ICBM is quite high, ranging from 1000-3300° K (Camac and Sepucha, 1976,365). This temperature gives rise to very small amounts of the thermally emitted UV radiation. Additionally, the magnitude of the emission is dependent on the wavelength of interest and composition of the fuel used. Although this process accounts for some UV emissions, most of the energy liberated in the thermal process is in the IR spectrum at about 1 to 3 μm.

Another possible thermal emission is that of thermal particulate radiation. This mechanism is characteristic of solid rocket engines in which small, unburned particles at high non-equilibrium temperatures radiate in the UV. A favored particle in solid rockets is aluminum. "In aluminum

containing propellants the rocket exhaust flow contains Al_2O_3 aluminum-oxide droplets and these particles are hot enough to radiate in the UV" (Camac and Sepucha, 1976,365). Furthermore, there are several other factors that suggest thermal particulate radiation in solid motors, in particular the continuum nature of the radiation and the similarity of the emission to solid body radiative behavior (Mcgregor and others, 1985,7).

Chemiluminescent Emissions. The chemiluminescent process is defined by Green as "non equilibrium free radiation resulting from chemical kinetic processes" (Green, 1966:249). Simply stated, chemiluminescence is the process of liberating photons as a result of a chemical reaction. The occurrence of this process in the exhaust plume is complicated and not completely understood.

Most exhaust plume gases contain substantial quantities of unburned fuel which give rise to large concentrations of carbon, hydrogen, and nitrogen, depending upon the type of fuel used. These unburned fuels give rise to chemical reactions which may produce UV emissions. Some of the more likely molecule reaction candidates for plume UV emission are as follows (Slack and others, 1983:18-25) :

$$O + O \Rightarrow O_2 + \text{photon (Schumann Runge band)}$$

$$N + O \Rightarrow NO + \text{photon (Beta and Gamma bands)}$$

$$CO + O \Rightarrow CO_2 + \text{photon (Blue flame continuum)}$$

$$H + OH + OH \Rightarrow H_2O + OH^*$$

$$OH^* \Rightarrow OH + \text{photon}$$

Table IV gives associated emission bands for these candidates for UV emission reactions.

TABLE IV

Emission Bands.
(Green, 1966; Shakleford, 1985)

Molecule	Mid UV Wavelength Band
OH	244 - 308 nanometers
CO_2	287 - 316 nanometers
CO	200 - 246 nanometers
NO	250 - 370 nanometers
O_2	244 - 437 nanometers

In almost all hydrocarbon flames, a strong UV emission can be found as a result of the OH radical formation by the fuel and oxygen combustion process (Validya and others, 1982:3357). As the fuel burns, an excited OH radical is created which emits an UV photon as it decays to the ground state. This electronically excited OH radical is believed to be a primary source of UV emission (Lyons and others, 1981:4-5).

Additionally, NO chemiluminescent may also contribute to the UV emission in a similar manner. Shakleford states that NO gamma radiation has been observed in all rocket plumes using nitrogen based fuel. Furthermore, he indicates that this emission should provide a useful UV plume signature (Shakleford, 1965:275).

In conclusion, there are many possible mechanisms which may contribute to the UV emission of the exhaust plume. In solid fuel engines, the thermal particulate emission as well as the chemiluminescence process is thought to provide the majority of the emission signature. In liquid fuel systems the chemiluminescence process appears to be the prime mechanism. Although the UV mechanisms are not well understood, they nevertheless produce UV radiation which may provide a useful plume signature.

Emission Data

One of the fundamental problems in the assessment of emission data has been the lack of accurate theoretical models to predict UV plume emissions. Determination of UV emissions have been attempted from three methods: 1) theoretical calculations, 2) static firing in altitude chambers and 3) flight tests. The first two methods have proven to be unreliable because of inadequate models and incomplete understanding of the UV emission mechanisms. Therefore, the empirical data from flight tests offers the most promising data (Gross and Montague, 1978:11).

In the past twenty years, a variety of programs have been conducted to measure UV emissions. More recent studies have focused interest on UV emissions in the OH band, 280-310 nanometers. Since virtually all propellants contain hydrogen in some form, it is thought that hydrogen reactions with surrounding oxygen will give rise to OH emissions in all exhaust plumes (Good, 1976:6). The two primary OH bands of interest are located at 281 and 306 nanometers.
One of the more extensive UV emission studies was conducted by T. A. Jacobs and R. R. Giedt. This study, conducted at Cape Canaveral over a period of about one year, monitored launches out of the Cape with ground based and airborne sensors. Their primary effort was to measure the UV emissions at 310 nanometers during launch from about 4 to 100 km. Data was collected at 310 nanometers with a 10 nanometer bandpass filter which covered the 306.4 nanometer OH emission band. The results of Jacob's findings are located in Table V and represent measurements made of various systems. Since a narrow bandpass filter was used in the measurement of the UV emissions, the values in Table V can be considered to be fairly conservative.

Other programs such as Project Trump Hitap and Project Chaser have conducted further study and measurements with varying results. However, the preciseness of the values is not the issue. The presented data is to be used only as a

guide to help bracket a range of intensity values that can be expected from Soviet ICBMs.

TABLE V

UV Emission Results
(1-100 km, In-band Intensities).
(Jacobs and others, 1965; Good, 1976)

System	Type Propellant	First Stage Thrust (lbs)	Intensity (W/Ster)
Thor-Delta	Lox +RP-1	200,000	10^2-10^3
Titan II	Hydrazine +N_2O_4	430,000	20-50
Polaris	Solid		10^2
Atlas-D	Lox +RP-1	336,000	10^2-10^3
Minuteman	Al +NH_4CLO_4	168,000	10^2-10^3

Unfortunately, UV measurements of Soviet ICBMs have not been reported in the open literature, and it seems unlikely any measurements have been conducted. Therefore, data on US systems will be used as a guide to suspected Soviet ICBMs values.

This extrapolation is fairly well founded for several reasons. First, like the US systems, all Soviet systems will probably contain some form of hydrogen in the fuel and will therefore exhibit OH chemiluminescence. Additionally, it is generally believed that UV emissions scale with the

amount of thrust produced (Good, 1976:6). Since Soviet ICBMs are generally larger and produce more thrust than US systems, it can be expected that Soviet ICBMs will exhibit large UV plumes and appear at least as bright in the UV as US ICBMs.

Summary

In summary, a generic ballistic missile trajectory has been developed, the threat has been investigated, and possible emission data has been estimated. For the purposes of this thesis, it will be assumed that Soviet ICBMs will have burnout altitudes ranging from about 80-400 km, that the UV plume emission is similar in nature to US plumes, and that the in-band intensity of these plumes will range from about 20 - 10^3 watts/steradian.

IV. Atmospheric Transmission

The atmosphere is responsible for several phenomena which directly affect the possibility of detecting a ballistic missile UV signature. Among these phenomena are that the atmosphere is a strong radiator in the UV spectrum and the inherent ability of the atmosphere to absorb UV radiation. Since the proposed detection system will be operating in the middle UV (200-300 nm), accurate assessment of the atmospheric effects must be made in order to evaluate system effectiveness. The latter of these phenomena will be discussed in the following chapter.

General Atmospheric Description

The earth's atmosphere is generally divided and studied in thermal layers. The first layer, which is also the most familiar, is the troposhere. This layer extends from about sea-level to 15 km. In the troposhere, which is home to all weather phenomena, the temperature decreases with increasing altitude, and the molecular number density is very high.

In the next layer, the stratosphere, the temperature is generally constant at -50° C. The stratosphere extends from the top of the troposhere to about 80 km. The only exception to this constant temperature is a layer from about 40-65 km in which there exists a warm zone. This warm zone is due to the presence of ozone which is an excellent

absorber of UV radiation (Abell, 1975:284). This is a rather beneficial effect since the ozone protects the lower altitudes from the potentially harmful UV radiation of the sun. However, it also hinders any space detection system operating in the UV from detecting UV radiation below the ozone layer.

Above the stratosphere is the thermosphere, ranging from 80 to 400 or 500 km, and included in this is the ionosphere. In these regions the atmospheric constituents and relatively low number densities do not seriously attenuate UV radiation, as later results will demonstrate.

The range of atmospheric altitudes that will be considered in this thesis is sea-level to 100 km. Later results will show that above 100 km the molecular and particulate number densities are small enough that their effect is negligible for calculation of UV radiation in the atmosphere. Furthermore, as previously stated, the primary absorber of UV, ozone, lies well below this altitude. Therefore, for purposes of simplicity it will be assumed that at 100 km the earth's atmosphere ends and space begins. The 1962 U.S. Standard Atmosphere will be the basic atmospheric model used for the earth's altitude below 100 km.

Attenuation Process

As the target UV radiation passes through the atmosphere, several processes take place which effectively

reduce the overall intensity of the signal. This attenuation process can be divided into basically two processes, absorption and scattering. The absorption process can be defined as a transformation of radiant energy into internal heat energy, whereas scattering is the process by which the electromagnetic energy is redirected with no loss of energy (Sears and others, 1984:726). Furthermore, the scattering process is highly dependent upon the relative size of the particles involved and the wavelength of incident radiation. Although these processes, absorption and scattering, are fundamentally different, the overall effect is the same, a reduction in overall target radiation received by a sensor.

The primary purpose of investigating these phenomena is to assess the degree of target signal attenuation in traversing the atmosphere. This in turn will determine the minimum altitude at which a given target signal can be detected.

Signal attenuation can be described mathematically by Lambert's law (Sears and others, 1984:726).

$$I_z = I_o \exp(-\mu z)$$

where I_z - target irradiance

I_o - original target irradiance

μ - absorption coefficient

z - distance traveled

This law assumes a large plane source and a homogeneous attenuating media. From the above formula, the signal transmission, $\tau \equiv I_z/I_o$, can be described by

$$\tau = \exp(-\mu z)$$

It should be noted that the transmission is only valid for a given distance z called path length. Furthermore, the absorption coefficient μ is dependent on the type of material the signal is traversing. In this case the medium is the atmosphere, and the absorption coefficient takes into account both forms of signal attenuation, scattering and absorption. When both the absorption and scattering components are combined in a single coefficient, they are commonly referred to as the extinction coefficient β_{EXT}.

Absorption. The atmosphere has many constituents which contribute to absorption at various wavelengths and at various altitudes. The primary absorbers of UV radiation in the earth's atmosphere are molecular nitrogen (N_2), molecular oxygen (O_2), atomic oxygen (O), and ozone (O_3) (Roble, 1986:24). Figure 1 shows the solar radiation absorption by the respective atmospheric constituents. For the particular wavelength band of interest, 200-300 nm, the majority of solar absorption is due to ozone (O_3). Although the ozone concentration in the atmosphere is very small, it is responsible for most of the UV absorption from 200-300 nm below about 100 km (Roble, 1986:24).

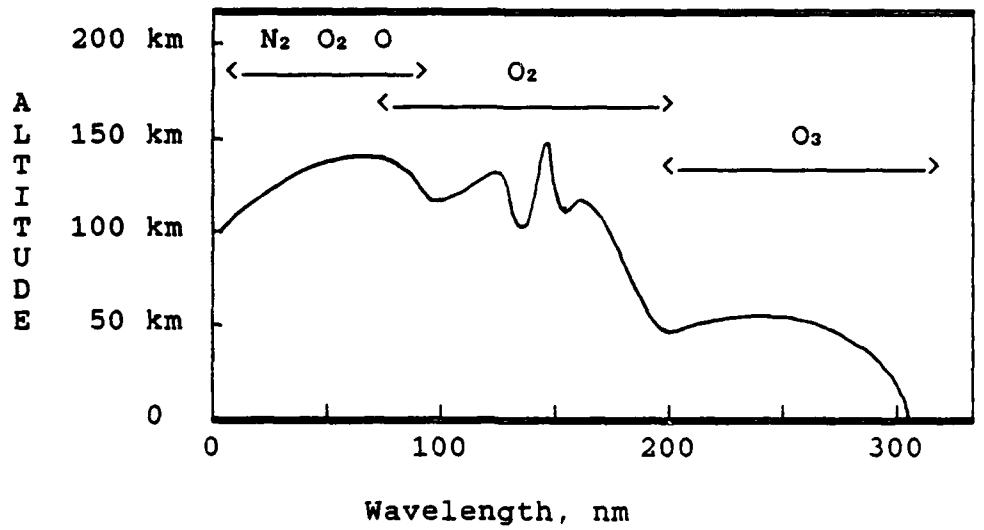

Figure 1. Solar UV Absorption
(Roble, 1986)

The primary UV absorption bands responsible are the Hartley band, which extends from about 200-320 nm, and the Huggins band, between 320-360 nm (Green, 1966:84). Although Figure 1 represents solar radiation absorption, it can be easily applied to the situation in which a target signal is propagating toward space. In any event, the presence of ozone in the atmosphere will limit the ability of any middle UV detection system to detect UV radiation at low altitudes because of its strong absorption characteristics.

In addition to the absorption process, there are several scattering mechanisms that will attenuate the target radiation as it propagates toward our space borne sensor. Among these mechanisms, the two most prevalent are Rayleigh scattering and aerosol (Mie) scattering.

Rayleigh scattering. Rayleigh scattering can be described as an elastic scattering of electromagnetic radiation by atmospheric atoms and molecules. In the ideal scatter process, the electromagnetic radiation does not lose any energy but is merely scattered in other directions. Rayleigh scattering occurs whenever the incident wavelength is much larger than the radius of the scattering particles. Since individual atoms and molecules have sizes on the order of 0.1-10 nm and the UV radiation wavelengths are on the order of 200-300 nm, it can be expected that Rayleigh scattering is a strong scattering mechanism. The Rayleigh scattering coefficient (Slater, 1980:194) can be described mathematically by the following relationship.

$$\beta_{\theta\lambda} = \frac{2\pi^2}{H\lambda^4}\left[n(\lambda)-1\right]^2\left(1+\cos^2\theta\right)$$

where

λ - wavelength

H - molecules per unit volume

$n(\lambda)$ - refractive index of molecules

θ - angle between incident and scattered flux

It should be noted that the Rayleigh coefficient is inversely proportional to the fourth power of the wavelength and the number density. It can be expected that middle UV radiation will be scattered significantly at lower altitudes

where the molecular number density is high. However, as altitude increases the number density will decrease and Rayleigh scattering will, therefore, also decrease.

Aerosols Scattering. Aerosols are a dispersion of solid or liquid particles that have become suspended in the atmosphere (Slater, 1980:195). Aerosol sizes can range from 10 nm for the smallest smoke particles to 10^5 nm for large raindrops. If the wavelength and particles of interest are approximately the same size, the scattering process is called Mie scattering. Unfortunately , Mie scattering does not lend itself to easy analysis. As Slater points out, Mie scattering is a complicated function of wavelength, particle size, refractive index and scattering angle (Slater, 1980:195). As a result, most aerosol scattering analysis is accomplished by using empirical models such as those found in the LOWTRAN 6 MODEL (Kneizys and others, 1983).

Summary. In the final analysis, the scattering process is similar to the absorption process in the respect that the end result is a decrease in total target radiation reaching the sensor. In context of the problem under investigation, the primary absorption of the target signal is by the ozone layer that lies at approximately 45-60 km. Below this altitude it is expected that the scattering processes will also be a significant contributor. However, since virtually all radiation is absorbed by the ozone layer, any scattering

attenuation will be insignificant in comparison to the absorption.

Additionally, above the ozone layer the particulate and molecular number density decreases rapidly, and it is expected that attenuation due to scattering in this region is negligible. Furthermore, the lack of ozone in large quantities above 60 km will eliminate any appreciable UV absorption in the wavelengths of interest, 200-300 nm.

Again considering Lambert's law and the extinction coefficient (β_{EXT}), it can be concluded that the extinction coefficient is composed of three separate attenuation coefficients: the attenuation coefficient due to Rayleigh scattering (β_r), the coefficient due to Mie scattering off of aerosols (β_a), and the coefficient due to ozone absorption (β_o). Therefore

$$\beta_{ext} = \beta_r + \beta_a + \beta_o$$

and the transmission can now be written as follows:

$$\tau = EXP(\beta_{EXT} Z) \quad or \quad \tau = \tau_r \tau_a \tau_o$$

Results of LOWTRAN Runs

In order to verify the above assumptions and to obtain UV transmission data for the signal-to-noise calculations, several computer runs were accomplished using the LOWTRAN 6 computer code. The particular code executed was specially

modified by Air Force Geophysics Lab to include updated analysis of the UV spectrum. Again, the primary purpose of these runs was to obtain transmission data so that ultimately the minimum signal detection altitude could be determined.

The following LOWTRAN inputs were selected for the LOWTRAN calculations (Kneizys and others, 1983):

1. The temperature, water vapor and ozone profiles from the 1962 U.S. Standard.
2. Rural aerosol model
3. Spring-summer season
4. Vertical viewing geometry

Using these assumptions, computer runs were accomplished at various path lengths. The path lengths were varied from space to 10 km altitude, space to 20 km , and so forth in increments of 10 km from space to the ground. Furthermore, data was collected over the wavelength of interest, 200 to 310 nm. A brief synopsis of the results will be presented here. For complete data see the output results located in the appendix. Table VI gives the a brief summary of the average transmittance over the given path length for the wavelength range of 200 to 310 nm.

TABLE VI

Average Transmittance at Various Path Lengths
200 to 310 Nanometers

Path Length	Average Transmittance
10 km to Space	.0163
20 km to Space	.0321
30 km to Space	.1367
40 km to Space	.4467
50 km to Space	.8869
60 km to Space	.9811
70 km to Space	.9975
80 km to Space	.9997
90 km to Space	1.000

As expected, it is noted that as the path length is increased from space through the ozone layer (40-60 km) there is a dramatic decrease in the UV transmitted. Table VII gives the, aerosol, ozone, and rayleigh transmission components for 250 nm. It can be seen from the table that above 60 km the transmission is essentially unity, and as previously assumed, scattering processes are negligible. Additionally, it can be concluded that the choice of aerosol and lower atmospheric models are not significant.

Table VII

Transmission at 250 Nanometers

Path Length	Transmission aerosol	ozone	rayleigh
10 km to Space	.988	.000	.475
20 km to Space	.996	.000	.855
30 km to Space	.999	.000	.966
40 km to Space	.999	.058	.991
50 km to Space	1.000	.763	.998
60 km to Space	1.000	.962	.999
70 km to Space	1.000	.996	.999
80 km to Space	1.000	.999	1.000
90 km to Space	1.000	1.000	1.000

Figure 2 represents the transmission as a function of altitude for wavelengths of 200, 250, and 300 nm. These results are similar to those of Stergis (Stergis, 1985:53).

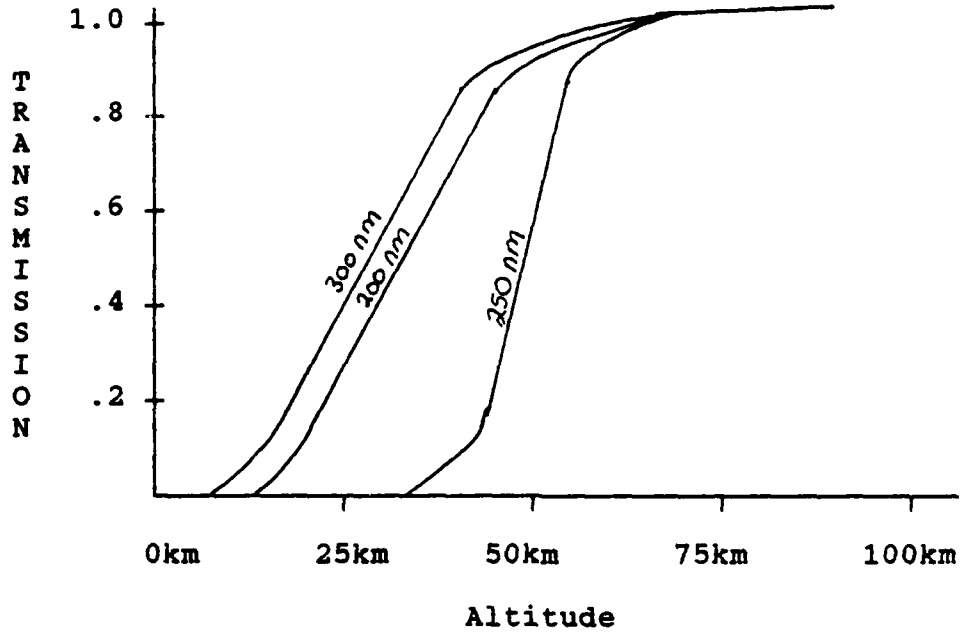

Figure 2. Transmission versus Altitude

Summary

In summary, the processes of signal attenuation, absorption and scattering have been discussed, and it has been shown how these processes are related mathematically to the attenuation of a target signal. From the results of the LOWTRAN data, it can be expected that any ICBM target signal may not be detectable below 60 km, roughly the upper boundary of the ozone layer. This assumes, of course, the absence of any background UV radiation which will be discussed in the next chapter.

V. Background Radiation

The purpose of this chapter is to explore the UV background emissions over which the ICBM plume signal must be detected. It is essential that the background be evaluated as accurately as possible because of the crucial role it plays in the calculation of the sensor signal-to-noise ratio.

The fact that the earth has characteristic emissions is not a recent discovery. Atmospheric emissions have been observed for thousands of years in the form of the visible aurora. It is, by comparison, only recently that the earth's airglow in the ultraviolet has become known.

The term airglow has come to commonly describe all atmospheric emissions and can be defined as a generally widespread, continuous glow of the earth's atmosphere (Hines, 1965:42). In contrast are the aurora phenomena which are more variable, highly localized, and generally occur at high latitudes. Although visible aurora and airglow phenomena have been studied from the ground for some time, it was not until high altitude experiments were conducted that the UV airglow was discovered.

The reason for the relatively recent discovery of UV airglow is that the ozone layer lies below the airglow UV emissions layers at about 100 km altitude. Since ozone absorbs most UV radiation in the 200-300 nm range,

measurements of UV airglow emissions in the middle UV from a ground experiment were virtually impossible. It was not until measurements above the atmosphere were made that the UV airglow in the middle UV became apparent. It is this UV airglow that will contribute virtually all of the background signal for our proposed sensor system.

Processes

High altitude observations have led to the discovery of an UV airglow over a wide range of wavelengths ranging from the far UV (100 nm) to the near UV (390 nm). To facilitate the description and study of airglow, it is commonly broken out into two distinct parts, the dayglow and nightglow.

Dayglow. Dayglow is defined as those emissions that occur while the atmosphere is irradiated by the sun. Dayglow results from the absorption of solar radiation by atmospheric constituents and the subsequent re-emission of the absorbed radiation. These spectral emissions are produced by resonant and fluorescent scattering of solar radiation, chemical and ionic reactions, and the photoelectronic excitation of atoms and molecules (Green and Barth, 1967:3975). Some of the emissions bands present in the dayglow are presented in Table VII.

TABLE VIII

Dayglow UV Emission Bands.
(McCormac, 1967:126)

Emission	Wavelength Band
Lyman alpha	121 nanometers
OI triplet	130 nanometers
NO gamma	200-300 nanometers
N_2	300-400 nanometers

From the data presented in Table VIII, it can be concluded that the primary source of background radiation during the day will be from NO gamma emission at 200-300 nm.

Nightglow. In contrast, nightglow emissions occur on the side of the earth away from the sun and are driven in part by the absorption of solar UV radiation during the day. As described by Hines, oxygen produced during the daytime in the forms of O and O_3 form a reservoir of energy which, by various slowly occurring reactions, can be transformed into airglow radiation at night (Hines, 1965:44). For our particular bandwidth of interest, 200-300 nm, the prominent nightglow feature appears to be in the Herzberg band of O_2 (Waters, 1972:51).

Measurements

Several measurement programs were undertaken during the early sixties to verify theoretical airglow calculations and

to increase the data available on the middle UV radiance of the earth. The majority of these measurements were done with the use of balloons (Dorian and Harshbarger) and high altitude aircraft such as the X-15 (Band and Block). Although these observations were a good first cut, they were incomplete in the context that they were done below the ozone layer. Observation of the middle UV radiance of the earth had to wait until sounding rockets and satellite experiments were accomplished.

In the late sixties and early seventies, several programs were undertaken to measure the earth's radiance in the UV from orbiting satellites. Such experiments were conducted on the Orbiting Astronomical Observatory (OAO-2) and the Orbiting Geophysical Observatory (OGO-IV) satellites. Both of these observations helped support the theoretical calculations of the earth's UV radiance. Figure 3 depicts the maximum spectral day (Gross and Montague, 1978:15) and night (Simmons, 1986:28) UV background of the earth based on current available data. Furthermore, Gross and Montague report that theoretical calculations and experimental results are in good agreement for the maximum UV radiance of the earth's atmosphere (Gross and Montague, 1978:13).

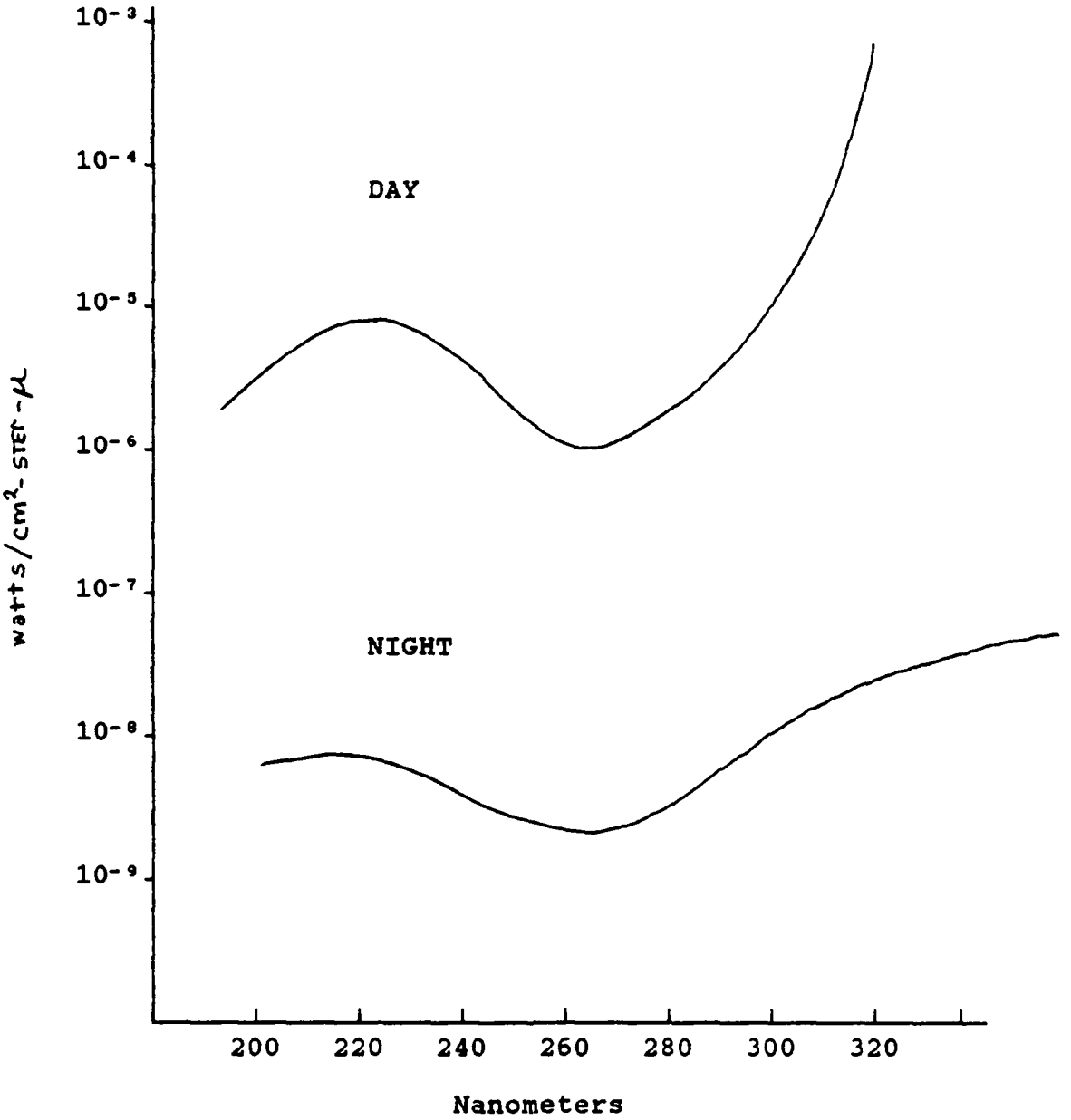

Figure 3. UV Spectral Background

Implicit in the data in Figure 3 is the assumption that there exists no spatial distribution of the UV background throughout the earth's atmosphere. Additionally Gross and

Montague (Gross and Montague, 1978:16) have stated that "no observations has been found which indicates short term intensity fluctuations or small spatial variations of as much as 10%."

In reality, it appears that little research has been conducted on the spatial characteristics of the UV airglow. Furthermore, Huffman has indicated that most experts consider the earth's spectral radiance to be spatially uniform (Huffman, 1986). However, it is interesting to note that on many UV images of the earth, such as those taken in the far UV spectrum by Apollo 16, there appears to be some spatial variations of the UV airglow (Carruthers,1972).

Although for most investigations the spatial uniformity of the UV airglow would be of debatable interest, it could be of important consequence in this application. If the UV airglow has considerable spatial characteristics, it could seriously affect the validity of the signal-to-noise analysis presented here, especially where borderline ratios are concerned. However, for purposes of this study, the background will be considered spatially uniform.

Additional Background Sources

There are many other sources of UV radiation, among which are the sun, galactic background, aurora phenomena, and terrestrial sources. Because of the downward geometry of the proposed sensor system, the sun and the galactic background should not present any direct addition to the

background. Furthermore, any terrestrial source (i.e. an UV laser) operating in the wavelength of interest will be absorbed by the ozone layer and therefore will not contribute to the background.

Moreover, the presence of a large aurora phenomena and its contribution to an increase in UV background is unclear. Although aurora spectral measurements have been made, the global occurrence of aurora has been mapped primarily in the visible and far UV. For the purposes of this study, the contribution of an aurora phenomena to the middle UV radiation background will not be considered.

VI. Sensor Requirements

In this chapter the requirements of the proposed sensor system will be outlined and discussed. Thus far in this thesis, all items discussed target signal, atmospheric transmission, and background are physical limitations which are beyond control. However, in considering the sensor system, the situation is reversed. There are several options in the design and operation of the system and, therefore, an attempt can be made to minimize the negative effects of the uncontrollable influences.

This chapter is organized as follows. First, a review of current and near future UV sensors will be reviewed. Second, the proposed sensor platform geometry will be described and discussed. Finally, the sensor considerations will be discussed and an overall picture of the proposed sensor system will be presented.

UV Sensors

Definitions. Before discussing possible candidate detectors, a brief review of detector system performance parameters would be helpful. Four important detector measurements that are important to this thesis are dark current, noise current, quantum efficiency, and gain. Each of these will be briefly defined and discussed.

Dark current can be defined as the detector output present when no input signal exists. There are several types of noise for ultraviolet detectors such as shot noise and thermal noise (Slater, 1980:408). Although each of these sources could be discussed at length, the key point is the effect of noise. In essence, the noise limits the sensitivity of the detector and increases the minimum threshold for signal detection. Therefore, it is desirable to have as low a dark current as possible. This is sometimes achieved by cooling the detector which also lowers the thermal noise. Obviously, this may be an expensive option in terms of weight and cost.

Another method of reducing dark current is by the physical design of the sensor system. For example, microchannel plates are designed specifically to amplify input currents with little additional noise produced. In conclusion, it is desirable to have small dark currents so as not to limit the sensitivity of the detector.

Quantum efficiency can be defined as the efficiency of a photocathode in converting photons into electrons. Any material used as a photocathode has a quantum efficiency which is a function of wavelength. Present day material quantum efficiencies for front surface electron generation are generally on the order of 20-30% (Viehmann, 1981:146-152). However, several new materials are being developed with quantum efficiencies reaching the 50% level (Reitz,

1986). Obviously, it is desirable to have quantum efficiencies as high as possible.

The last measurement to be discussed is gain. Gain is a function of the detector and the associated electronics. Gain represents the amount of amplification of the signal generated by the detector. In some sensors, such as those containing microchannel plates, overall gains as high as 10^6 have been achieved. Although high gains are desirable, it should be noted that amplification occurs for not only the target current but background and dark currents as well.

Current Devices. Photon detectors in general can be divided into two basic types, non-imaging flux detectors and imaging detectors. A non-imaging detector is capable of indicating whether an electromagnetic signal is present, but is not able to preserve the two-dimensional image of the radiative scene or any spatial information of the scene (Coleman, 1981:3693).

The detection of an ICBM launch and subsequent tracking requires the detector to be an imaging type detector rather than a simple one-dimensional flux detector. Since the objective of the proposed system is to detect and track ICBMs, a survey of UV imaging sensors has been made.

From the reviewed literature, the two most promising sensors include either the microchannel device and/or the charged couple device. These devices will be reviewed in the following paragraphs.

Charged-Couple Devices. The solid state devices which show much potential in the application at hand are the charged-couple-devices (CCD). In essence, a CCD is a very small microchip which contains a large array of individual detectors or pixels. The largest detector currently in use is an 800 x 800 pixel CCD imager with a pixel size of 15 x 15 μm built in silicon material for the space telescope (Blouke, 1980:3318; Blouke, 1983:608).

In order to make a CCD device responsive to UV photons, it must be coated with a photoemissive compound. Coronene ($C_{24}H_{12}$) is one such chemical compound sensitive to UV photons (Viehmann, 1981:147). In operation, a UV photon strikes the coronene which absorbs the UV photon. This, in turn, produces a photon in the visible wavelength which is subsequently detected by the detector array (Blouke, 1980:3318). There are also several other materials that can be used in place of coronene such as liumogen and doped acrylic. Although these materials offer good sensitivity in the UV, the effective quantum efficiency of a coated detector is generally not more than 30% (Viehmann, 1981:151).

Additionally, the CCD detector offers many advantages such as light weight, small size, low power consumption, and low dark current. However, there are several disadvantages including low sensitivity in the UV, necessity to cool the detector to obtain low dark currents, and the lack of any

electrical gain. The microchannel plate overcomes some of these shortcommings.

Microchannel Plate. The microchannel plate is essentially an imaging electron multiplier. It is described by Coleman as a bundle of closely packed glass tubes, similar to fiber optics, which have been fused together. Each glass tube (microchannel) is typically 12 to 25 μm in diameter and approximately 1 millimeter in length (Timothy, 1985:1068-1069). The key advantage of a microchannel plate is that each microchannel can support secondary electron emissions, which produces a large electro-optical gain.

The operation of the device is as follows. First, a photocathode substance sensitive to the UV photons of interest is deposited on the face of the microchannel plate. When a UV photon strikes the photocathode, an electron is generated and ejected into the glass tube. Each glass tube is slightly curved, with a potential across the tube, so the electron strikes the wall of the tube and several more electrons in addition to the original are produced. As the process continues down the tube, more and more electrons are produced. This results in a gain at the back of the plate of 10^5 or 10^6 electrons (Coleman, 1981:3699-3670; Timothy, 1985:1071).

There are currently, several photocathode materials used for coating microchannel plates. Among the more familiar are cesium iodide (CsI) and cesium telluride

(Cs_2Te). A promising new material that has received much attention recently is galium-aluminum-nitride (GaAlN). GaAlN is a photocathode material which is expected to have a significantly improved quantum efficiency as well as sharper high wavelength cutoff. Studies thus far indicate that quantum efficiencies may approach the 50% (Reitz,1986). Figure 4 shows the respective frequency responses and quantum efficiencies of Cs_2Te and GaAlN.

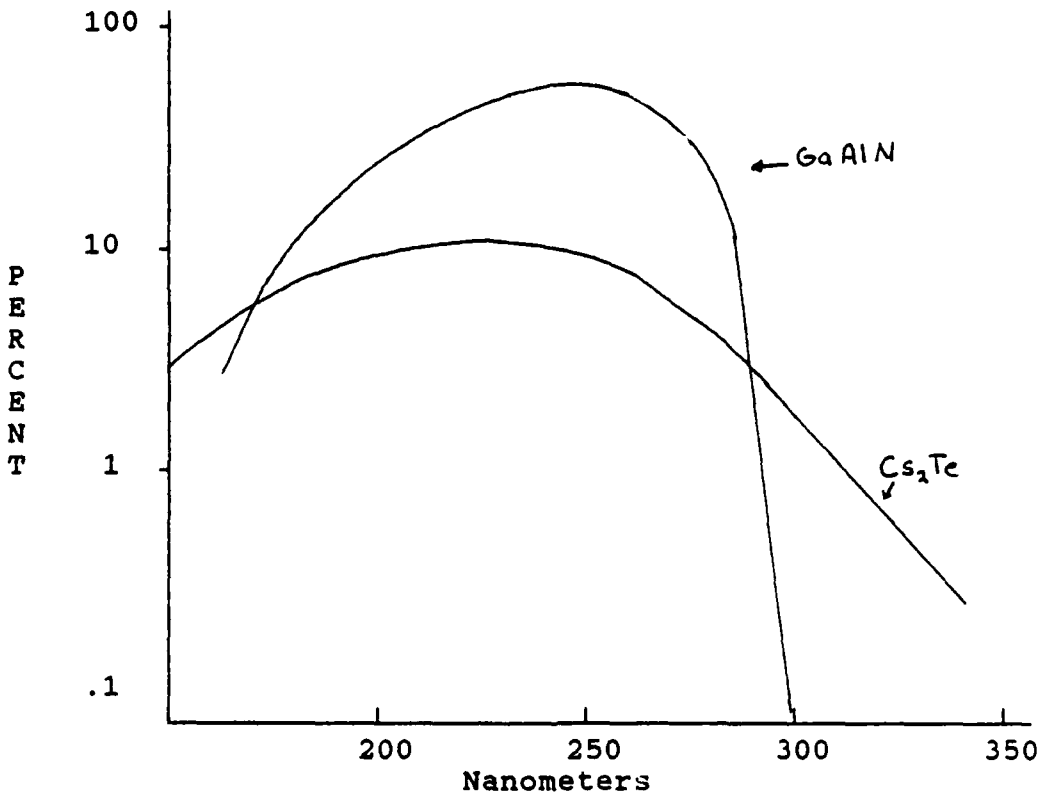

Figure 4. Cs_2Te and GaAlN Quantum Efficiencies

It should be emphasized that an ideal detector should have a high quantum efficiency and zero out-of-band

response. Thus the detector is responsive only over the bandwidths of interest. In comparing Cs_2Te and GaAlN, Figure 4 shows that GaAlN offers both a higher quantum efficiency and sharper cutoff for the bandwidth of interest, 200-300 nm. This characteristic makes GaAlN quite attractive for the proposed sensor system.

Several microchannel plates with large detector arrays have been built and tested. One current detector array is a 256x1024 pixel array built for flight on the Balloon-Borne Ultraviolet Stellar Spectrograph. Future development plans include a 1024x1024 pixel array with 25x25 μm pixels and a 4096x4096 pixel array with 12x12 μm pixels to be completed in late 1986 (Timothy, 1985:1070).

In conclusion, both the microchannel plate and the CCD detectors offer suitable detector characteristics. Both are light in weight, small in size, offer very small individual detector elements, and offer low dark currents, all of which make them suitable candidates for the desired application.

Geosynchronous Orbit

The first problem to address in any remote sensing application is a description and analysis of the conditions and geometry under which the remote sensing is to take place. For the problem at hand, remote sensing of ICBM plumes, current sensing philosophy can be used as a reference point. Currently, remote sensing of ICBM launches is accomplished by satellites stationed in geosynchronous

orbit (Space Handbook, 1985:12-1). The reason for this particular philosophy rests in the advantages offered by the geosynchronous orbit.

Advantages. There are several key advantages to this particular orbit. First is the fact that a geosynchronous satellite, in effect, remains stationed over a fixed area of the earth. This allows for continuous surveillance of an area of interest. The second advantage is the reduced technical requirements for an elaborate steering system to keep the sensor system looking at the area of interest. Third is the advantage of being able to view large areas of the earth with a single satellite. The final advantage involves the issue of survivability. Although it is not impossible to destroy a satellite stationed in a geosynchronous orbit, these satellites are relatively immune to current anti-satellite weapons.

Disadvantages. The geosynchronous orbit is not, however, without several disadvantages. Among these are the long distance over which a sensing system must detect the desired signal. Since a target's signal strength at the sensor varies inversely with the square of the distance, this places a fundamental limitation on the maximum distance over which a given target signal can be detected. Another disadvantage is the limitation in the amount of weight that can be launched to a geosynchronous orbit. This weight limitation dictates the overall size of any geosynchronous

satellite system which in turn limits the size and geometry of any optical system on board.

In consideration of the advantages and disadvantages of the geosynchronous orbit, it will be assumed that any future ICBM launch detection satellite will be placed in this orbit in line with current philosophy. Therefore, it will be assumed in this thesis that the proposed sensor system will be placed in and must operate from a geosynchronous orbit.

Sensor Platform Geometry

Figure 5 depicts the geometry of a proposed system stationed at a geosynchronous orbit. From such an orbit, coverage of an entire hemisphere of the earth may be possible.

By analysis of the satellite geometry and the target motion, several key elements can be derived such as the coverage requirements and the maximum integration time of the sensor system.

Satellite Coverage. From Figure 5 the sensor or total field-of-view, that necessary for hemispheric coverage of the earth, can be derived. Once the coverage requirements have been calculated, the imaging resolution requirements determine the focal length as well as the detector size for the proposed system. However, there will obviously be a physical limit on the maximum size of the detector array and the focal length because of their spacecraft application.

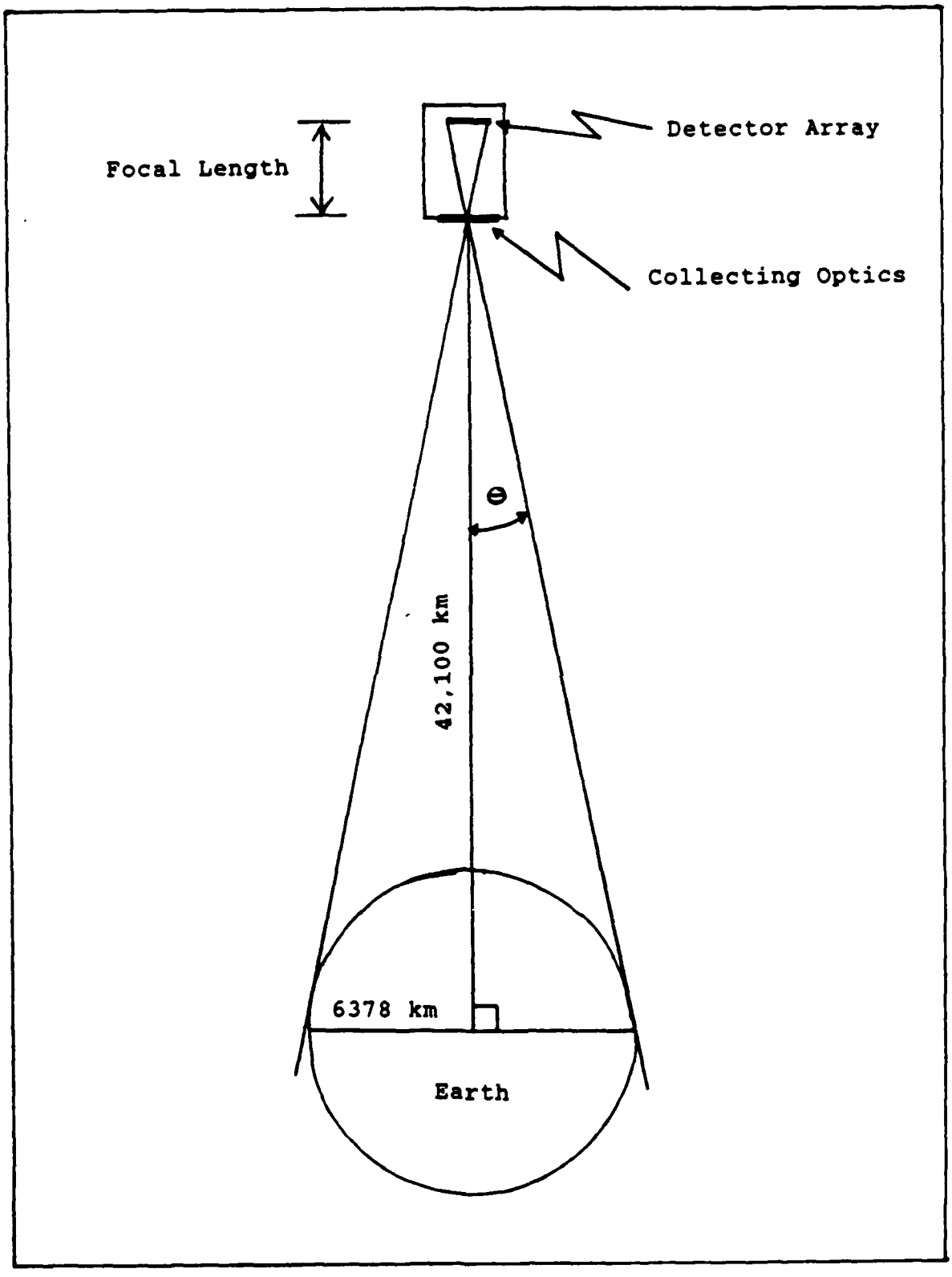

Figure 5. Geosynchronous Satellite Geometry

First, an analysis of the total sensor coverage will be accomplished.

The sensor half angle field-of-view, theta ( ), can be derived by use of simple geometry and the physical characteristics of the orbit, see Figure 5.

$$\Theta = \text{ARCTAN} \left[\frac{R_e}{r} \right]$$

where

R_e = radius of earth

r = distance from earth center

By substituting the earth radius (6378 km) and the distance to geosynchronous orbit from the earth's center (42,100 km) into the above equation, theta is found to equal 8.75° or 0.15 radians. Additionally, the total field-of-view solid angle subtended (Ω) can be calculated from the following equation (Slater, 1980:530).

$$\Omega = 2\pi (1 - \cos\Theta) \approx \pi \Theta^2$$

Using the value of 0.15 radians calculated above, the total solid angle subtended is calculated to be approximately 0.071 steradians.

Sensor considerations

Before any detailed discussion of the sensor system can be accomplished, the nature of the target and background

signals must be investigated. Since the earth is continuously bathed in a UV airglow, the background source can be considered an extended source. This implies that the UV background will completely fill the field of view (FOV) of the sensor at all times. On the other hand, the target source can be considered as a point source. Generally speaking, a source can be considered a point source if its distance from the detector is ten times its linear dimension. This is obviously the case in point, because typical measured UV plume sizes are 1000 m^2 which are much smaller than their range of 35,880 km (Gross and Montague, 1978:18).

Signal-to-Noise. In order to gain an understanding of those factors which contribute to an increase in signal-to-noise ratio (SNR), the contents of chapter two are reviewed. Recall that the SNR is defined as follows:

$$SNR = \frac{I_T}{I_N}$$

where

I_T = target current

I_N = noise current

Furthermore,

$$I_N = (I_T + I_B + I_D)^{1/2} (e/\tau_d)^{1/2}$$

with

I_T = target current

I_B = background current

I_D = dark current

T_d = dwell time

e = 1.6 x 10^{-19} coulombs

Ideally, it would be desirable to operate the proposed system in the absence of any unwanted signal. If this were possible, the limiting factor on SNR would be the dark current inherent in the system. Unfortunately, the case under consideration must detect the incoming target signal amid the presence of background radiation. In this case, the background and target currents will be shown to be considerably larger than dark current (I_B, I_T >> I_D), and the proposed detection system is background limited. Therefore, the SNR may be approximated by

$$SNR \approx \frac{I_T (T_d)^{1/2}}{e \left[I_B + I_T \right]^{1/2}}$$

In order to achieve a high SNR, the background current (I_B) must driven as small as possible while maintaining the target current (I_T) constant. From inspection of the target current and the background current equations (Chapter II), it can be seen that in order to decrease I_B without a resulting decrease in I_T, the detector FOV must be decreased. This is intuitively appealing since any decrease

in the detector solid angle (Ω_i) will decrease the number of background photons striking an individual detector, resulting in lower background current and hence the SNR,

$$SNR \propto \frac{I_T (T_d)^{1/2}}{(\Omega_i)^{1/2}}$$

Additionally, the SNR can be increased by increasing the sensor dwell time, T_d. In the ideal situation in which the target does not move, long sensor dwell times with small Ω_i will yield a high SNR. However, when the target is in motion, the maximum sensor dwell time is dependent on the detector FOV and, hence, Ω_i.

Dwell Time. The sensor integration time or dwell time is the amount of time the detector can be allowed to "look" at the target area. If the dwell time is too short, the target signal will not have time to be distinguished from the background. On the other hand, if the target is in motion and the dwell time is too long, the target will have time to move out of the FOV of the detector during the integration time. Therefore, it is desired for the dwell time to be as long as possible, but not so long as to allow the target to move out of the FOV of an individual detector. As a result, an upper limit on the dwell time can be established:

$$T_d \leq \frac{\Theta_i}{V_T}$$

where

Θ_i = instantaneous field-of-view

V_T = angular velocity of the target relative to the sensor

Since, the detector solid angle subtended (Ω_i)

$$\Omega_i \approx \Theta_i^2$$

for small angles and square detectors, the upper limit on the dwell time can be approximated by

$$T_d \lesssim \frac{\Omega_i^{1/2}}{V_T}$$

Again returning to the SNR equation developed previously, the above approximation for the dwell time can be substituted into the equation for SNR.

$$SNR \propto \frac{I_T (T_d)^{1/2}}{(\Omega_i)^{1/2}} \approx \frac{I_T}{(\Omega_i)^{1/4}}$$

This analysis indicates that the SNR is still dependent on the detector fields of view, Ω_i . It can be concluded that small detector fields-of-view dominate in the attempt to suppress the unwanted background. This in turn drives the maximum time over which signal integration can occur. If long integration times are required, then the detector

field-of-view must be increased with a corresponding increase in background.

As mentioned previously there are several physical constraints that must be considered in the design of a detector system. Among these constraints are the detector size spacing, the detector array size, the design focal length, and the area of the collecting optics. Each of these will be discussed.

Detector size limitations. The individual detector size spacing is driven by two factors--the detector field of view and the focal length. In order to cover an entire hemisphere of the earth, it has been seen that the required sensor FOV has a plane angle value of approximately 0.3 radians (Θ). The detector field-of-view (θ_i) for an individual detector can be calculated from the following equation:

$$\theta_i = \frac{\Theta}{N}$$

where

Θ = total FOV = 0.3 radians

N = number of detectors

For a large detector array size of 1000x1000, recall from the previous discussion that several on the order of this magnitude have been built, the θ_i is calculated to be approximately 3×10^{-4} radians. Recall that the larger the array size (number of detectors), the smaller the Ω_i possible. If various focal lengths are assumed, the

detector size/spacing can be derived from the following equation:

$$d = (\Theta_i) F$$

where

d = detector size spacing

Θ_i = detector field-of-view

F = focal length

By using the above relationship, detector size spacing was calculated for focal lengths of 1 to 5 meters. The results, located in Table IX, indicate that the required detector size/spacing is well within current technological capabilities (Detector size/spacings as small as 15 μm have been demonstrated (Blouke and others, 1983)).

TABLE IX

Detector size spacing
for various Focal Lengths

Focal Length	Detector size
1 meter	300 μm
2 meter	600 μm
3 meter	900 μm
4 meter	1.2 mm
5 meter	1.5 mm

Detector Array Limitations. The total physical dimension of the detector array is another limitation that must be considered because of uniformities of photocathodes and the maximum chip size. Analysis of the array

limitations is similar to the above detector size analysis. The detector array size is dictated by the focal length and the total FOV desired.

$$d_A = \Theta F$$

where

d_A = detector array size

Θ = total field-of-view desired

F = focal length

From the previous analysis, it was found that the total Θ desired was approximately 0.3 radians. Again assuming reasonable values for the focal length, array sizes can be calculated. Table X show results for focal lengths from 0.1 to 2 meters with a total FOV of 0.3 radians.

TABLE X

Array sizes for
Various Focal Lengths

Focal Length	Detector array size
2 meter	60 cm
1 meter	30 cm
0.5 meter	15 cm
0.3 meter	9 cm
0.1 meter	3 cm

Several conclusions can be drawn from Table X. First, the detector array size required with focal lengths of one meter or more present a formidable technological challenge. For example, at one meter the detector size required is 30

cm x 30 cm or 900 cm^2. Current technology can provide detector arrays in the range from 20 to 50 mm, but arrays on the order of tens of centimeters have yet to be developed. This places an upper .imit on the focal length of about 17 cm in those cases where the total FOV coverage is desired with a single array. Hence, several chips may need to be integrated together to get entire earth coverage at the required spatial resolution.

Another key technological problem involves the photocathode material. Assuming an array of large size can be built, there is an additional problem of uniformly coating the device with a suitable photocathode material.

Collecting Optics. There is another fundamental sensor limitation involving focal lengths and the size of the collecting optics. In any detection system it is generally desired to have large collecting optics. This is driven by the fact that the larger the collecting optics, the more area available for collection of target photons. However, a problem can arise if large collecting optics and short focal lengths are required. In general a limitation exist between the collecting optics diameter and the focal length. This relationship is expressed as follows:

$$\frac{F}{D} \gtrsim \frac{1}{4}$$

where

F = focal length

D = diameter of optics

This results from the fact that $F \cong 1/2\,R$ for $D \ll R$ and $D \leq 2R$ (Sears and others, 1984:751-754). For example, in the case where the desired focal length is 0.5 meters, the diameter of the collecting optics must be less than or equal to 2 meters. Collecting areas of one meter are probably an upper limit for applications on a space platform. A one meter collecting area results in focal lengths of not less than approximately 15 centimeters.

The discussion thus far has described the physical limitations that must be considered in the design of any sensor system. The analysis has been done with an implicit assumption that the total FOV must be covered by a single detector array. However, this may not be possible nor desirable.

Recall that the overall objective in sensor design is to achieve as high a SNR as possible within the limitations discussed above. Furthermore, it has been shown that high SNR can be achieved by requiring high resolution. However, since the minimum detector size is fixed by technology, the only way to achieve increasing resolution is by increasing the focal length.

Recall that Θ_i , detector size, and the focal length relationship can be expressed by using the small angle approximation.

$$\Theta_i = \frac{d}{F}$$

where

d = detector size

F = focal length

Current individual detector sizes are on the order of 15 μm. If a focal length of 5 meters is assumed, an Θ_i of approximately 3×10^{-6} radians results. However, a 5 meter focal length would require a detector array size on the order of 2.25 m^2, which is clearly unrealistic with current technology. Therefore, if long focal lengths are required to achieve the needed resolution, the total Θ of the sensor will be necessarily reduced.

For the case in point, detector array sizes on the order of 20 mm are feasible. If a 5 meter focal length is assumed, the approximate Θ is 4×10^{-3} radians, clearly less than the required Θ of 0.3 radians for total hemispheric coverage. Obviously, tradeoffs between detector size, focal length, and detector array dimension must be considered in any sensor design.

VII. Results

This chapter will discuss the results and analysis of the signal-to-noise calculations for the proposed sensor system. The chapter is organized as follows: First, there is a brief discussion of the computer program written to aid in the calculations of the signal-to-noise ratios. Next, a brief review of the data presented thus far is discussed followed by an outline of the baseline sensor system used in calculating the results. Finally, the results will be presented and discussed.

Signal-to-Noise Computer Calculations. In order to facilitate the calculation of the signal-to-noise ratios, a Fortran computer program was developed and used. Briefly, the program performs the necessary integrations and calculations of the current and signal-to-noise equations found in chapter II. The program uses the following data inputs:

1. Target intensity, I_λ
2. Background radiance, L_λ
3. Detector gain, G
4. Quantum efficiency, η
5. Optics transmission, τ_o
6. Atmospheric transmission, τ_a
7. Sensor focal length, F
8. Detector size, d
9. Target range, r
10. Area of collecting optics, A_r
11. Detector dwell time, T_d

The following output is generated from the above listed inputs: background and target current, background and target electron counts, and overall signal-to-noise ratios. Appendix A contains a listing of the Fortran code as well as a more detailed program description.

Review of Data

Before a baseline sensor system is described, a brief review of the data presented thus far will be beneficial.

Target characteristics

1. Burnout altitudes of 80 to 400 km.
2. In-band intensities of 20 to 10^3 w/ster.

Atmospheric transmission

1. Minimum of 1% (path length 10 km to space).
2. Maximum of 100% (path length 90 km to space).

Background radiance in spectral bandpass, 200 nm $\leq \lambda \leq$ 320 nm

1. Maximum value can have any of the daytime values, ranging from 10-6 to 10-3 watts/cm2-ster-μm depending on λ .
2. Minimum values can have any of the nighttime values, ranging from 10-9 to 10-6 watts/cm2-ster-μm depending on λ .

Sensor considerations

1. Minimum individual detector sizes ranging from 25 to 12 μm.
2. Maximum detector array sizes in the range of 15 mm to 50 mm (1000x1000).
3. Possible focal lengths of 0.5 to 10 m.
4. Collecting area of not more than 1 m^2.
5. Quantum efficiencies ranging from 10% to 30% with possibilities in the near future of approaching the 50% level.
6. Maximum gains of 10^5 to 10^6.

A baseline sensor system, target, and viewing geometry were assumed from the above data remaining within the capabilities of current technology. The parameters of this assumed system are as follows:

Detector size - 15 μm
Array size - 20 x 20 mm (1000x1000)
Focal length - 5 meters
Collecting area - 1 m^2
Transmission of optics - 95%
Transmission of atmosphere - 1.0
Gain - 10^5
Detector - GaAlAs with a maximum efficiency of 30% in-band
Target values - 10 and 1000 w/ster in-band
Target distance - 35,800 km, altitude of a geosynchronous satellite sensor system
Spectral bandpass - 240 to 290 nanometers

It should be noted that atmospheric transmission (τ_a), optic transmission (τ_o), gain (G), and target spectral intensity (I_λ) are all functions of wavelength, but for simplicity are assumed constant over the wavelengths of interest.

Sample Calculations

Several values can be immediately calculated from the baseline parameters discussed above. The resolution of the system characterized as a solid angle subtended, Ω_i , is determined from the detector size and focal length. For the baseline sensor with a detector size of 15 μm and a focal length of 5 m, the detector field-of-view, Ω_i , is approximately 2.8 x 10^{-11} steradians. Since the minimum detector size is fixed by technology, the only way to

increase resolution, if needed, is to increase the sensor focal length.

In addition to resolution, the overall FOV of the sensor system can be calculated from the detector array size and focal length. The baseline system, a 5 m focal length and 20 mm detector array size, dictates a total field-of-view, Ω ,of the sensor system of approximately 4 x 10^{-3} radians. Since Ω required for total earth coverage is 0.3 radians, more than one detector array must be used in order to achieve the total coverage.

Recall that the signal-to-noise ratio (SNR) for a sensor operating in the pulse counting mode can be approximated as follows:

$$SNR \approx \frac{(I_T/e)\,(T_d)^{1/2}}{(I_B/e + I_T/e)^{1/2}}$$

where

I_T = target current

I_B = background current

T_d = dwell time

e = 1.602 x 10^{-19} coulombs

and

$$I_T = \frac{e\,A_r}{h\,c\,r^2} \int_{\lambda_1}^{\lambda_2} I_\lambda\, \tau_o\, \tau_a\, G\, \eta\, \lambda\, d\lambda$$

$$I_B = \frac{e\,A_r\,\Omega_r}{h\,c} \int_{\lambda_1}^{\lambda_2} L_\lambda\, \tau_o\, \tau_a\, G\, \eta\, \lambda\, d\lambda$$

Using the framework of the baseline system and an in-band target value of 10 w/ster with day background values (see Figure 3), the target current, I_T, and background current, I_B, can be calculated provided a detector bandpass is assumed.

The above functions were integrated (from 240-290 nm) for the target and background currents. The results of these integrations are as follows:

Target current, $I_T = 3.14 \times 10^{-11}$ amps

Count rate, $I_T/e = 1.96 \times 10^{8}$ e^- /sec

and

Background current, $I_B = 3.45 \times 10^{-11}$ amps

Count rate, $I_B/e = 2.16 \times 10^{8}$ e^- /sec

The only value still unknown for signal-to-noise calculation is integration time (T_d). Recall that the maximum integration time is determined by the resolution of the system and the target velocity. As calculated previously, the baseline resolution is approximately 10^{-11} steradians. Furthermore, since any "useful" ICBM's trajectory must remain below approximately 8 km/sec to prevent orbit insertion, this value was used as a maximum expected ICBM velocity.

If a target velocity of 8 km/s is assumed, the maximum integration time allowed is approximately 0.015 seconds.

Therefore, a baseline integration time of 1 msec, well within the maximum allowable, was used.

Using the above discussed values for I_B, I_T, and integration time, the SNR was calculated to be approximately 300. Recalling that a large (i.e. greater than 10) signal-to-noise ratio indicates that a signal can be detected amid the background, it can be concluded that an UV plume of 10 w/ster would be detectable under the discussed conditions.

In the framework of the described baseline system, signal-to-noise ratios were calculated using in-band target values of 10 and 500 w/ster, an integration time of 1 msec, and a bandpass of 240 to 290 nm. The results of these baseline calculations are depicted in Table XI.

TABLE XI
Baseline System Target Result Matrix

	10 w/ster	500 w/ster
Day	305	3070
Night	442	3105

It is interesting to note that both day and night conditions yield practically the same SNR. This results from the fact that with the small field-of-view of the baseline sensor, the target current is the same order of magnitude as the background current.

Out of band rejection calculations. Implicit in the assumed bandwidth, 240 to 290 nm, is the assumption that the detector has a square wave response. In order to evaluate this assumption, SNR calculations were derived for three cases. The detector response was assumed to be a square wave in the first case, a GaAlAs detector (see Figure 4) in the second case, and similar to Ce_2Te (see Figure 4) in the final case. In each case, the background and target currents were integrated from 220 to 380 nm using an in-band target of 10 w/ster to evaluate the detector response on SNR. The results of these calculations are presented in Table XII.

TABLE XII
SNR for Various Detector Responses

	Type Response		
	Square	GaAlAs	Ce_2Te
SNR	230	263	30

As seen in Table XII, the assumption of square wave response does not seriously affect the outcome of the calculations when a GaAlAs detector is used. On the other hand, when a Ce_2Te detector response curve is used, the square wave assumption is not acceptable. The relatively slow decrease in detector response at the higher wavelengths seriously affects the out-of-band rejection of the detector. As a result, the SNR is degraded significantly. However,

since the baseline detector system assumed a GaAlAs detector, the square wave detector response assumption can be considered valid.

Presentation of Results

In order to explore the feasibility of the proposed sensor system, signal-to-noise ratios were calculated for various conditions using the framework of the baseline sensor system. Calculations were done to trade-off the effects of resolution, integration time, and target altitude on SNR.

SNR versus Resolution. Figure 6 shows the result on SNR from varying resolution, or detector field-of-view, Ω_i, using an in-band target intensity of 10 w/ster, day and night spectral background radiances (Figure 3), the baseline model, an integration time of 1 msec, and a minimum value of $\Omega_i = 10^{-11}$ steradians.

Likewise, Figure 7 depicts the result on SNR from varying resolution, Ω_i, using an in-band target intensity of 500 w/ster. In both Figures, the solid triangles indicate the values of SNR from the baseline system.

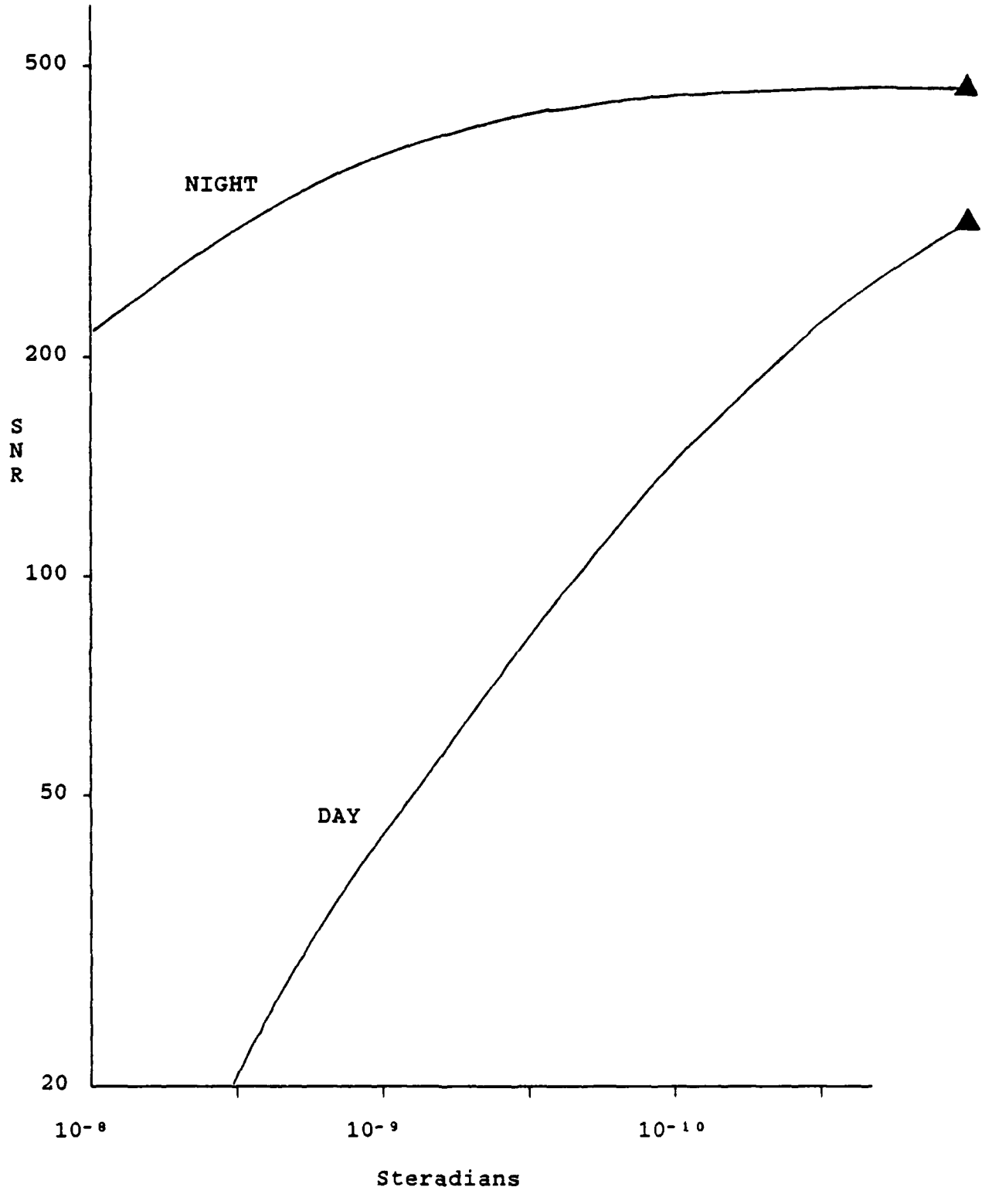

Figure 6. SNR versus Resolution (10 w/ster)

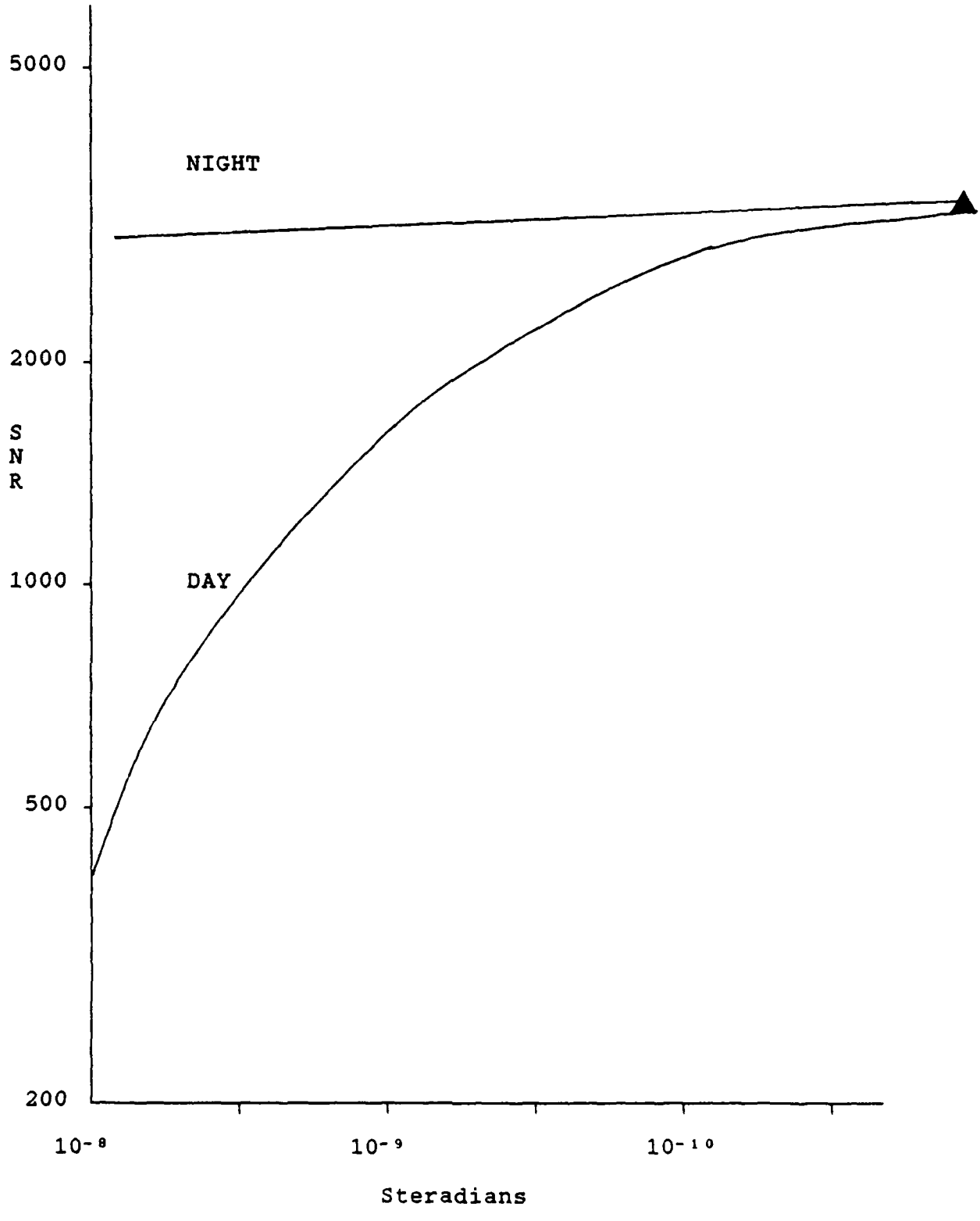

Figure 7. SNR versus Resolution (500 w/ster)

Furthermore, several conclusions can be drawn from the previous two figures. First, during both day and night viewing conditions, acceptable SNRs are possible for resolutions of 10^{-9} steradians or better. For the upper limit, in-band target intensities of 500 w/ster, SNRs are in excess of 200 for resolutions of 10^{-8} steradians during both day and night conditions.

For the lower in-band target intensities of 10 w/ster, the baseline system provides good SNRs for both day and night conditions. However, during day viewing conditions, the SNR decreases to marginal values with decreasing resolutions approaching 10^{-8} steradians. For example, a resolution of 10^{-8} steradians results in a SNR of approximately 8, which is expected since the larger resolution allows for more background signal to enter the field-of-view.

In summary, the baseline sensor resolution of approximately 10^{-11} steradians provides for acceptable SNR for in-band target intensities of 10 and 500 w/ster under both day and night conditions.

SNR versus Integration Time. Figure 8 shows the result on SNR from varying integration time, T_d, using an in-band target intensity of 10 w/ster, day and night spectral background radiances (Figure 3), and the baseline model. Likewise, Figure 9 depicts the result on SNR from varying integration time using an in-band target intensity of 500

w/ster. In both figures, the solid triangles indicate the values of SNR calculated using the baseline system.

Note from the two figures that for both day and night viewing conditions, increasing the integration time increases the SNR values as expected from the SNR equation. Recall, however, that although high SNR can be achieved by long integration times, there is a limit to the maximum integration time dictated by the target motion and required resolution.

In each of the above cases, a maximum integration time is imposed by the resolution (θ_i'), target velocity (V_m), and target distance (r). The relationship of these values is as follows:

$$T_d \leq \frac{\theta_i'}{\left(\frac{V_m}{r}\right)} = 15 \text{ msec}$$

By adhering to the restrictions of the above equation, the target can be assured of not moving out of the detector field-of-view during the sensor integration time.

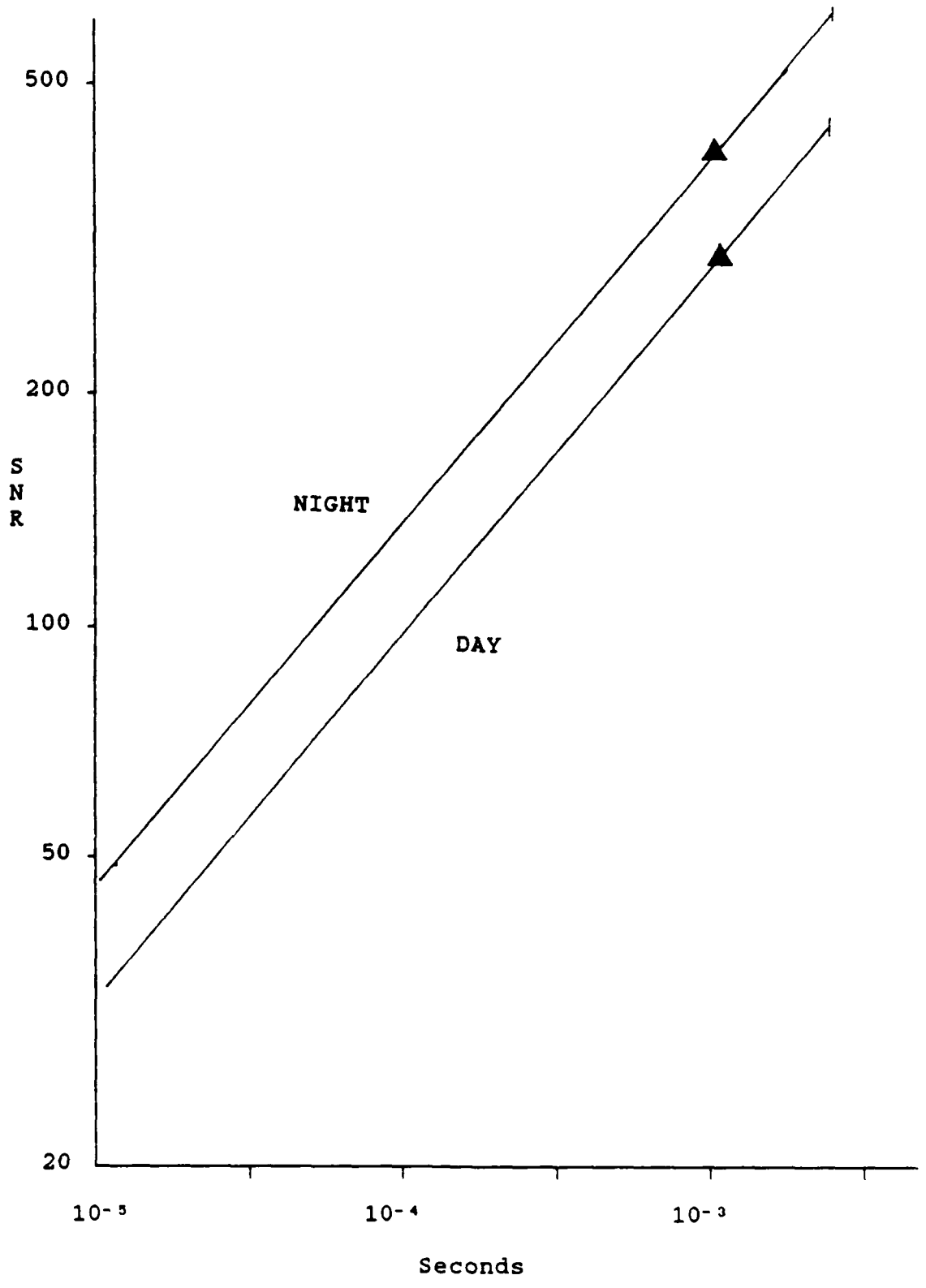

Figure 8. SNR versus Integration Time (10 w/ster)

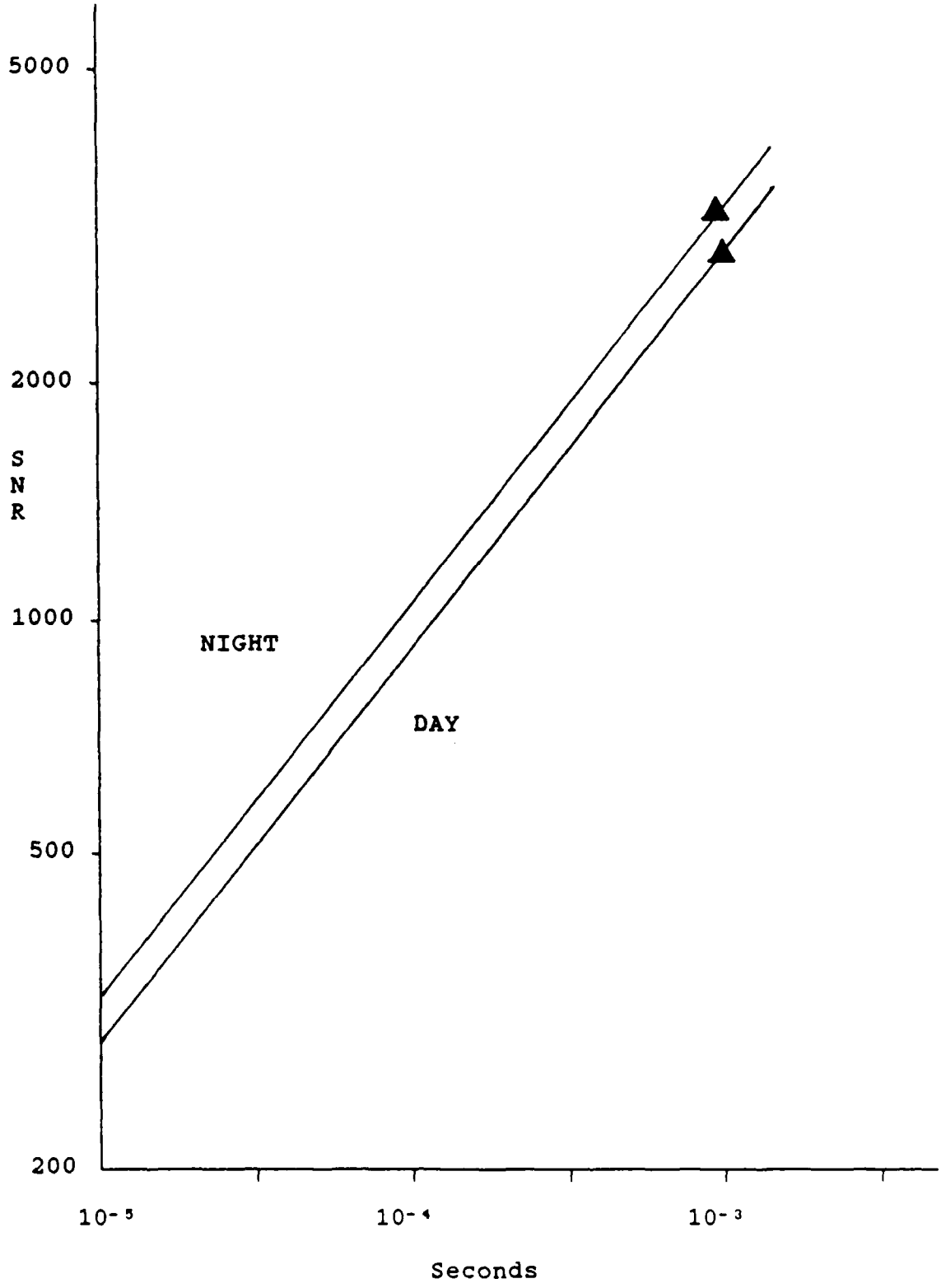

Figure 9. SNR versus Integration Time (500 w/ster)

SNR versus Altitude. The final two figures, Figure 10 and Figure 11, depict the SNR versus target altitude relationship for target intensities of 10 and 500 w/ster. This data was calculated by using the framework of the baseline sensor and the spectral atmospheric transmission results from the LOWTRAN output (See Appendix B).

From both of the figures, it can be seen that for both 500 and 10 w/ster targets there is a drop in SNR which occurs at about 40 to 60 km. This drop is due to the ozone layer absorption of the target signal as discussed in Chapter IV. From this data, it can be concluded that ICBM UV plumes can be detected down to about 35 to 40 km depending on their in-band intensities. However, below this altitude the ozone will effectively mask an UV plume from a spaceborne sensor system.

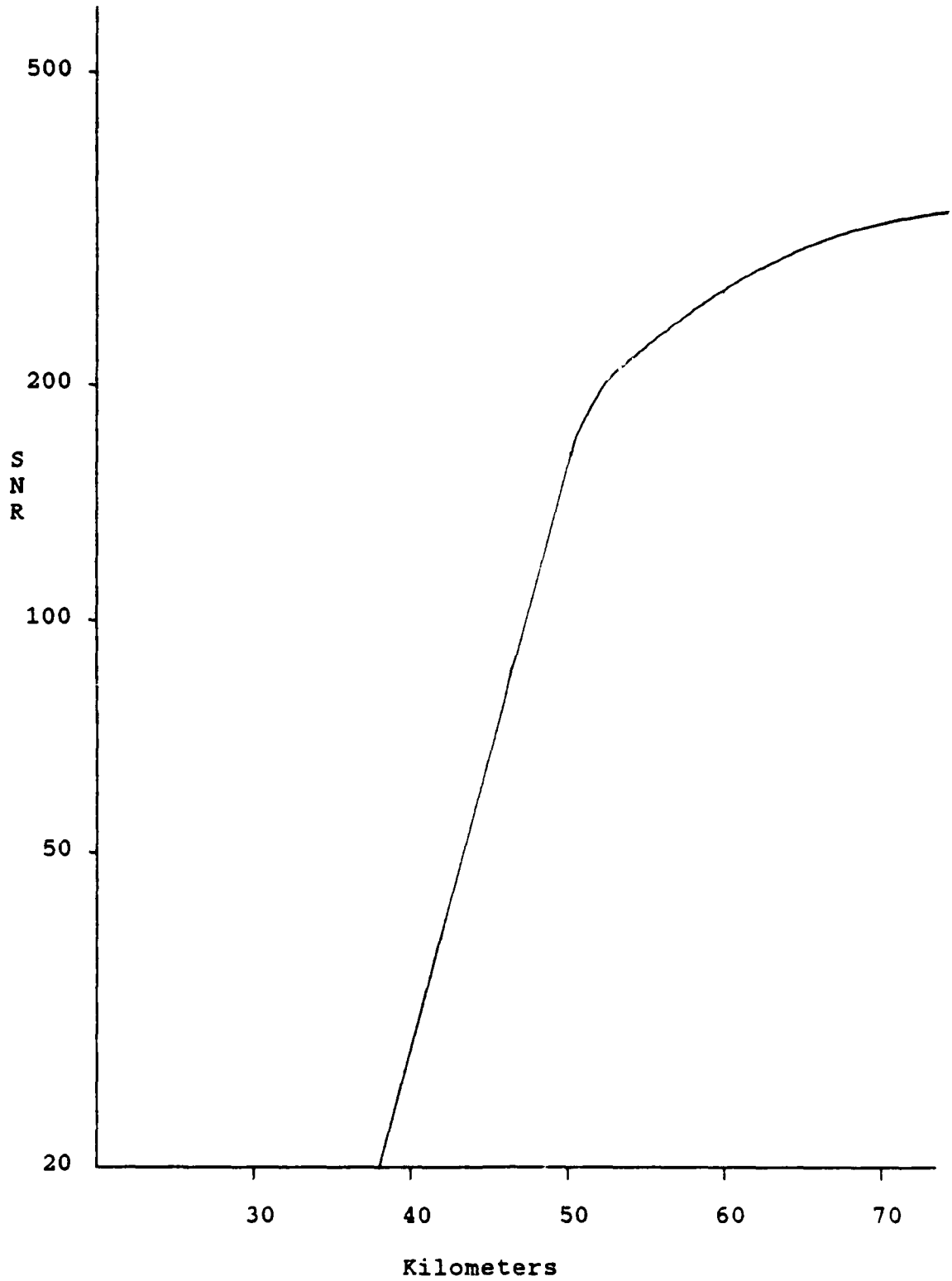

Figure 10. SNR versus Target Altitude (10 w/ster, day)

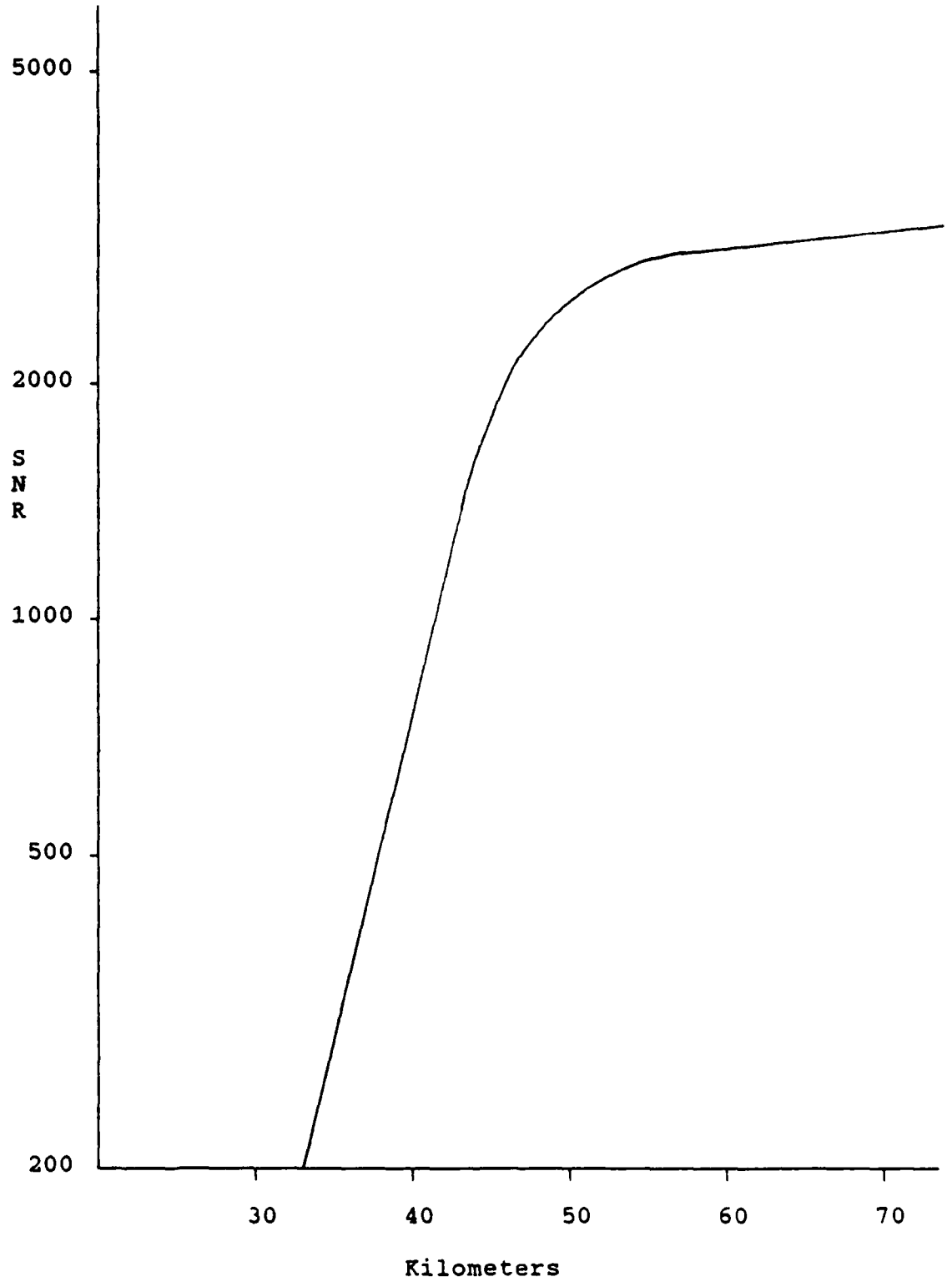

Figure 11. SNR versus Target Altitude (500 w/ster, day)

VIII. Summary, Conclusions and Recommendations

The data presented and analyzed in this thesis have been aimed at addressing the following question: Can the UV plumes of an ICBM in the boost phase be detected from a space platform? In order to answer this question, analysis was undertaken to investigate the signal-to-noise ratios for plume intensities in the range of 10 to 500 watts/ster which were representative of the measurements of current ICBMs and similar booster systems.

Summary of Results

Night Conditions. Under night viewing conditions, analysis indicates that sufficient target signals exist for detection of an UV plume with in-band intensities on the order of 10 watts/ster when using the baseline system. Therefore, virtually all ICBM systems discussed in Table V would be detectable.

Day Conditions. During daytime conditions, the UV background of the earth is approximately three orders of magnitude greater than night values. This reduces the possibility of detecting those UV plumes with relatively small intensities using large fields-of-view. During the day, the baseline sensor system is capable of detecting in-band plume intensities of as little as 10 watts/ster with integration times of 1 msec provided resolutions of at least

10^{-9} steriadians are used. Once again, in the framework of the proposed baseline system, the ICBM systems discussed in Table V would be detectable.

Minimum Altitude. Minimum altitude for signal detection is driven by the ozone layer, which is an excellent absorber of middle UV radiation. During worst case viewing (daytime), adequate SNR can be maintained using the baseline system for intensities of 10 w/ster down to an altitude of approximately 45 km. Similarly, intensities in the range of 500 w/ster are detectable to approximately 35 km.

Conclusions

This investigation has revealed that the current state of UV detector technology and the magnitude of most current ICBM plume intensities are sufficient to allow for detection from a geosynchronous sensor system. The current state of UV technology is adequate enough to support the needed resolution from geosynchronous orbit, but entire earth coverage is not possible with a single detector array.

Additionally, it has been found that current ICBM launch profiles provide adequate time for detection of their UV plumes during the boost phase. However, with the deployment of fast burn ICBMs exhibiting high accelerations and low burnout altitudes, the time allowable for launch detection becomes short. During the initial acceleration of a fast burn ICBM, the ozone layer will help to mask the

signal from any spaceborne system, and this, coupled with the relatively low booster burnout altitudes, will result in relatively little time for launch detection. In this scenario, the usefulness of an UV launch detection system requires further evaluation.

Recommendations

Recommendations from this work stem primarily from the shortcomings discovered. As expected, further study and measurement of the background and target radiation would enhance the accuracy of the analysis. Although much research has been conducted to accurately measure the UV background radiance, the spatial distribution of the UV airglow is a subject that has received little attention. Research into this area would be helpful to produce an accurate model of the UV airglow distribution.

Additionally, a more accurate assessment of the spectral content of UV exhaust plumes is needed. A systematic measuring program for determining the magnitude and spectral content of ICBM UV plumes would greatly enhance the evaluation of any proposed sensor systems.

Furthermore, as discussed in this work, any sensor design requires trade-off considerations between detector size, focal lengths, pixel sizes, and so forth. Any further research into this subject should include a a detailed study to evaluate sensor design/trade-off alternatives.

Lastly, a study should be undertaken to investigate the possibility of an infrared/ultraviolet detection system consisting of an infrared sensor for launch detection and a UV sensor system for target tracking.

APPENDICES

Appendix A

Computer Program

This appendix will give a brief description of the computer program written to calculate signal-to-noise ratios. The program was written in Microsoft Fortran for execution on a Zenith Z-150 PC or any other IBM compatible PC.

The program requires the support of two external files, DSNDATA and SNRESLT.DTA. DSNDATA contains the input data that is currently in use. SNRESLT.DTA contains the generated output and is essentially a copy of the results presented to the user at the terminal.

The program was designed to be user friendly and uses a menu driven philosophy. Furthermore, it will allow the user to change any or all of the inputs interactively.
Once the user has specified the needed inputs, the program will approximate the given functions using a Newton divided difference-interpolating polynomial and integrate over the wavelength range specified by using a Romberg numerical integration technique. Both the Newton interpolation polynomial and the Romberg integration algorithms can be found in Carnahan, Luther and Wilkes book, Applied Numerical Methods.

Inputs

The following are a list of the user defined inputs.

1. Wavelength in meters
2. Target intensities in watts/steradian.
3. Background radiance in watts/meter-steradian.
4. Detector gain.
5. Quantum efficiency.
6. Transmission of optics.
7. Atmospheric transmission.
8. Sensor focal length in meters.
9. Detector size in meters.
10. Target range in meters.
11. Collecting optics area in square meters.
12. Look angle in radians.
13. Detector dwell time in seconds.

When entering data, the user should first define the wavelength range over which the data is defined. The inputs for items 2 thrcugh 7 will allow the user to input twenty data points over the given wavelength range. From these data points, a numerical approximation will be made by using a Newton divided difference algorithm. The algorithm was tested and found to behave well for exponential and logarithm functions provided the range of input data was not too large (i.e. attempting to approximate an exponential over the range of 1 - 500 using 20 data points).

Additionally, the program allows the user to select the desired sensor inputs, items 8 through 12 above. Once inputs are made, they may be saved in DSNDATA for future use if desired.

Outputs

Once data input is accomplished, the program will request the bandpass over which integration is desired. Obviously, an integration should not be attempted beyond the range of defined values as invalid results would result. Once the integration has been accomplished, the following results are output.

1. Background current in amps.
2. Target current in amps.
3. Background photon count.
4. Target photon count.
5. Signal to noise ratio.
6. Echo check of input values.

The first five items above will be displayed at the user's terminal. Additionally, these results as well as an echo check of input values will be printed to the output file, SNRESLT.DTA to provide a hard copy capability.

Variable Names

All variables used were implicitly typed as double precision throughout the program. Therefore, any variable, regardless of its first letter, is double precision unless explicitly typed otherwise. The following is a list of the major variables and their meanings.

ARRAY VARIABLES

XAXIS(20) - input values for wavelength range
CB(20) - divided differences table for background
CG(20) - " " " for the gain
CQ(20) - " " " for the quantum efficiency
CO(20) - " " " for optic transmission
CA(20) - " " " for atmospheric transmission
CT(20) - " " " for target values

BKY(20) - input background values
GY(20) - " gain values
QY(20) - " quantum efficiency values
OY(20) - " optic transmission values
TY(20) - " target values
AY(20) - " atmospheric transmission values

OTHER VARIABLES AND CONSTANTS

C - speed of light constant
H - Planck's constant
E - electron charge constant
SANGLE - solid angle
FOCAL - focal length of sensor
DSIZE - detector size
RANGE - range from detector to sensor
THETA - look angle
RAREA - area of receiver optics
DTIME - dwell or integration time

PROGRAM LISTING

```
      PROGRAM DSGN
      IMPLICIT REAL*8 (A-Z)
C
      COMMON XAXIS(20),CB(20,20),CG(20,20),CQ(20,20),
     -  CO(20,20),CA(20,20),CT(20,20),BKY(20),GY(20),QY(20),
     -  OY(20),TY(20),AY(20),C,H,E,SANGLE,FOCAL,DSIZE,
     -  RANGE,THETA,RAREA,DTIME
C
C
      INTEGER J
      OPEN(1,FILE='DSNDATA')
      OPEN(6,FILE='SNRESLT.DTA',STATUS='NEW')
C
      CALL LOADATA
10    CALL MENU
      READ(*,*) J
      IF (J.GT.5) GOTO 10
      GOTO(20,30,40,50,60),J
20    CALL TSHOW
      GOTO 10
30    CALL SHOW
      GOTO 10
40    CALL CRUNCH
      GOTO 10
50    CALL SAVES
      GOTO 10
60    WRITE(*,101)
101   FORMAT(///,' SAVE CURRENT PARAMETERS ? ',/
     -          ' 1 FOR YES   2 FOR NO',/)
      READ(*,*) J
      IF (J.EQ.1) CALL SAVES
      STOP
      END
C
C
C  MAIN MENU
C
      SUBROUTINE MENU
      WRITE(*,80)
80    FORMAT(1X,//////,20X,'M A I N     M E N U',//,20X,
     -  '1.DISPLAY CURRENT PARAMETERS',/,20X,'2. EDIT PARA',
     -  'METERS',/,20X,'3. CALCULATE SIGNAL TO NOISE',/,20X,
     -  '4. SAVE CURRENT PARAMETERS',/,20X,'5. EXIT',//,20X,
     -  'ENTER CHOICE (1-5)'/////////)
      RETURN
      END
C
C  FUNCTION BACKGROUND
C
      REAL*8 FUNCTION BACK(X)
      IMPLICIT REAL*8 (A-Z)
      COMMON XAXIS(20),CB(20,20),CG(20,20),CQ(20,20),
     -  CO(20,20),CA(20,20),CT(20,20),BKY(20),GY(20),QY(20),
     -  OY(20),TY(20),AY(20),C,H,E,SANGLE,FOCAL,DSIZE,
     -  RANGE,THETA,RAREA,DTIME
C
      REAL*8 X
      BACK=FNEWT(1,X,IER)
      RETURN
      END
C
C  FUNCTION GAIN
C
      REAL*8 FUNCTION GAIN(X)
      IMPLICIT REAL*8 (A-Z)
      COMMON XAXIS(20),CB(20,20),CG(20,20),CQ(20,20),
     -  CO(20,20),CA(20,20),CT(20,20),BKY(20),GY(20),QY(20),
     -  OY(20),TY(20),AY(20),C,H,E,SANGLE,FOCAL,DSIZE,
     -  RANGE,THETA,RAREA,DTIME
C
      REAL*8 X
      GAIN=FNEWT(2,X,IER)
      RETURN
      END
C
C  FUNCTION TARGET
C
      REAL*8 FUNCTION TGT(X)
      IMPLICIT REAL*8 (A-Z)
      COMMON XAXIS(20),CB(20,20),CG(20,20),CQ(20,20),
     -  CO(20,20),CA(20,20),CT(20,20),BKY(20),GY(20),QY(20),
     -  OY(20),TY(20),AY(20),C,H,E,SANGLE,FOCAL,DSIZE,
     -  RANGE,THETA,RAREA,DTIME
C
      REAL*8 X
      TGT=FNEWT(5,X,IER)
      RETURN
      END
C
C  FUNCTION QUANTUM
C
      REAL*8 FUNCTION QUANT(X)
      IMPLICIT REAL*8 (A-Z)
      COMMON XAXIS(20),CB(20,20),CG(20,20),CQ(20,20),
     -  CO(20,20),CA(20,20),CT(20,20),BKY(20),GY(20),QY(20),
     -  OY(20),TY(20),AY(20),C,H,E,SANGLE,FOCAL,DSIZE,
     -  RANGE,THETA,RAREA,DTIME
C
      REAL*8 X
```

```
      POINT FNEWT(X,IER)
      RETURN
      END
C
C  FUNCTION OPTICS
C
      REAL*8 FUNCTION OPTIC(X)
      IMPLICIT REAL*8 (A-Z)
      COMMON /AXIS/ XAXIS(20),CB(20,20),CG(20,20),CO(20,20),CO(20,20),
     -  CA(20,20),CT(20,20),BY(20),GY(20),DY(20),DY(20),TY(20),
     -  AY(20),C,H,E,SANGLE,FOCAL,DSIZE,RANGE,THETA,RAREA,DTIME
C
      REAL*8 X
      OPTIC=FNEWT(4,X,IER)
      RETURN
      END
C
C
      REAL*8 FUNCTION ATM(X)
      IMPLICIT REAL*8 (A-Z)
      COMMON /AXIS/ XAXIS(20),CB(20,20),CG(20,20),CO(20,20),CO(20,20),
     -  CA(20,20),CT(20,20),BY(20),GY(20),DY(20),DY(20),TY(20),
     -  AY(20),C,H,E,SANGLE,FOCAL,DSIZE,RANGE,THETA,RAREA,DTIME
C
      REAL*8 X
      ATM=FNEWT(6,X,IER)
      RETURN
      END

C
C  INTEGRATION FUNCTIONS
C
      REAL*8 FUNCTION GRTB(X)
      IMPLICIT REAL*8 (A-Z)
      COMMON /AXIS/ XAXIS(20),CB(20,20),CG(20,20),CO(20,20),CO(20,20),
     -  CA(20,20),CT(20,20),BY(20),GY(20),DY(20),DY(20),TY(20),
     -  AY(20),C,H,E,SANGLE,FOCAL,DSIZE,RANGE,THETA,RAREA,DTIME
C
      REAL*8 X
C
      GRTB=BAC(X)*OPTIC(X)*ATM(X)*QUANT(X)*GAIN(X)*(X*1.0E6)
      RETURN
      END
C
      REAL*8 FUNCTION GRTT(X)
      IMPLICIT REAL*8 (A-Z)
      COMMON /AXIS/ XAXIS(20),CB(20,20),CG(20,20),CO(20,20),CO(20,20),
     -  CA(20,20),CT(20,20),BY(20),GY(20),DY(20),DY(20),TY(20),
     -  AY(20),C,H,E,SANGLE,FOCAL,DSIZE,RANGE,THETA,RAREA,DTIME
C
      REAL*8 X
C
      GRTT=TGT(X)*OPTIC(X)*ATM(X)*QUANT(X)*GAIN(X)*(X*1.0E6)
      RETURN
      END
C
C
C   CRUNCH THE NUMBERS
C
      SUBROUTINE CRUNCH
      IMPLICIT REAL*8 (A-Z)
      COMMON /AXIS/ XAXIS(20),CB(20,20),CG(20,20),CO(20,20),CO(20,20),
     -  CA(20,20),CT(20,20),BY(20),GY(20),DY(20),DY(20),TY(20),
     -  AY(20),C,H,E,SANGLE,FOCAL,DSIZE,RANGE,THETA,RAREA,DTIME
C
      REAL*8 A,B,ERR
      INTEGER ERROR
C
      CALL DTABLE(ERROR)
      WRITE(*,150) XAXIS(1),XAXIS(20)
  150 FORMAT(///////,15X,'ENTER DESIRED BANDPASS INTERVAL',/,
     -   15X,'RANGE FROM ',E8.3,/,15X,'          TO ',E9.3,///)
  154 WRITE(*,155)
  155 FORMAT(///,15X,'ENTER LOWER BOUND (REAL*8)')
      READ(*,*) A
      IF ((A.LT.XAXIS(1)).OR.(A.GT.XAXIS(20))) GOTO 154
  158 WRITE(*,160)
  160 FORMAT(///,15X,'ENTER UPPER BOUND (REAL*8)')
      READ(*,*) B
      IF ((B.LT.XAXIS(1)).OR.(B.GT.XAXIS(20))) GOTO 158
      IF (A.GT.B) GOTO 154
C
      CALL CALSN(A,B,0.0001D0)
      RETURN
      END
C
C  ITEGRATION ROUTINE
C
      REAL*8 FUNCTION ROMB(F,A,B,ERROR,MAXIT)
      IMPLICIT REAL*8 (A-Z)
      INTEGER MAXIT,I,J,I,N
      REAL*8 A,B,ERROR,H,ARG,NEWTAB,F
      OLD1,OLD2,DEMON,RMBO,R(50)
      EXTERNAL F
C
C
      H=B-A
      R(1)=(F(B)+F(A))*(H/2.0D0)
      N=1
      DO 100 I=2, MAXIT
      OLD1=R(1)
      NEWTAB=0.0D0
      ARG=A+H/2.0D0
```

```
C
      DO 200 J=1,N
      NEWTAB=NEWTAB+F(ARG)
      ARG=ARG+H
200   CONTINUE
C
      R(1)=(OLD1+H*NEWTAB)/2.0D0
      DENOM=4.0D0
      DO 300 I=2,K
      OLD2=R(I)
      R(I)=R(I-1)+(R(I-1)-OLD1)/(DENOM-1)
      OLD1=OLD2
      DENOM=DENOM+4.0D0
300   CONTINUE
      H=H/2.0D0
      N=2*N
      IF (DABS(R(K)-R(K-1)).LE.ERROR) GOTO 600
      WRITE(*,*) K
100   CONTINUE
      K=MAXIT
600   ROMB=R(K)
      RETURN
      END
C
C   CALCULATE SIGNAL TO NOISE
C
      SUBROUTINE CALSN(A,B,ERR)
      IMPLICIT REAL*8 (A-Z)
      COMMON XAXIS(20),CB(20,20),CG(20,20),CQ(20,20),
     - CO(20,20),CA(20,20),CT(20,20),BKY(20),GY(20),QY(20),
     - QY(20),TY(20),AY(20),C,H,E,SANGLE,FOCAL,DSIZE,
     - RANGE,THETA,RAREA,DTIME

      REAL*8 A,B,ERR,IT,IB,SN,HLP,ROMB,IGRTB,IGRTT
      EXTERNAL GRTB,GRTT
C
      HLP=ROMB(GRTB,A,B,ERR,50)
      WRITE(*,901) HLP
901   FORMAT(////,1X,' INTEGRATION OF GRTB = ',D20.11)
902   FORMAT(1X,'                  GRTT = ',D20.11)
      IB=(HLP*COS(THETA)*SANGLE*E*RAREA)/(H*C)
      HLP=ROMB(GRTT,A,B,ERR,50)
      WRITE(*,902) HLP
      IT=(HLP*COS(THETA)*E*(RAREA/RANGE**2))/(H*C)
      SN=((IT/E)*SQRT(DTIME))/SQRT((IT/E)+(IB/E))
      WRITE(*,905) IB,IB/E,IT,IT/E
905   FORMAT(//,'  IB = ',D20.11,' COUNT= ',D20.11,
     -        /,'  IT = ',D20.11,' COUNT= ',D20.11)
      WRITE(*,910) SN,ERR,ERR
910   FORMAT(// ' SIGNAL TO NOISE IS ->> ',D20.11,//,
     - ' ESTIMATED ACCURACY',/,' BACKGROUND - ',D10.5,/,
     -                       '      TARGET - ',D10.5,//)
C
      CALL PRNTIT(A,B,IB,IT,SN,ERR)
      WRITE(*,*) ' ENTER 1 TO CONTINUE'
      READ(*,*) J
      RETURN
      END
C
C   TSHOW ROUTINE
C
      SUBROUTINE TSHOW
      IMPLICIT REAL*8 (A-Z)
      COMMON XAXIS(20),CB(20,20),CG(20,20),CQ(20,20),
     - CO(20,20),CA(20,20),CT(20,20),BKY(20),GY(20),QY(20),
     - QY(20),TY(20),AY(20),C,H,E,SANGLE,FOCAL,DSIZE,
     - RANGE,THETA,RAREA,DTIME

      INTEGER I
      WRITE(*,260)
260   FORMAT(1X,/,'      *********      DATA FOR',
     - ' APPROXIMATING  FUNCTIONS     **********')
      WRITE(*,265)
265   FORMAT(1X,'WAVELTH     TARGET     BACKGRD      GAIN  ',
     - '     ONTEFF     OPTICS     ATMOSHR',/,' METERS      ',
     - 'W/ST        W/M2-S       VALUE      VALUE     PERCENT',
     - '    PERCENT')
      DO 275 I=1,20
      WRITE(*,270) XAXIS(I),TY(I),BKY(I),GY(I),QY(I),
     -             QY(I),AY(I)
270   FORMAT(1X,D8.3,2X,D8.3,3X,D8.3,4X,D8.3,2X,D8.3,
     - 3X,D8.3,2X,D8.3)
275   CONTINUE
C
      WRITE(*,281)
281   FORMAT(1X,' ENTER 1 TO CONTINUE')
      READ(*,*) A
      WRITE(*,282)
282   FORMAT(//,20X,'*****   SENSOR DATA   *****',//)
      WRITE(*,285) FOCAL
      WRITE(*,287) DSIZE
      WRITE(*,289) RANGE
      WRITE(*,291) THETA
      WRITE(*,293) RAREA
      WRITE(*,295) SANGLE
      WRITE(*,297) DTIME
285   FORMAT(15X,'  FOCAL LENGTH = ',D20.11,'  METERS',/)
287   FORMAT(15X,' DETECTOR SIZE = ',D20.11,'  METERS',/)
289   FORMAT(15X,'  TARGET RANGE = ',D20.11,'  METERS',/)
291   FORMAT(15X,'         THETA = ',D20.11,'  RADIANS',/)
293   FORMAT(15X,' RECEIVER AREA = ',D20.11,'  METERS ',
     - SQR',/)
295   FORMAT(15X,' REC SOLID ANG = ',D20.11,'  STER',/)
297   FORMAT(15X,'     DWELL TIME = ',D20.11,'  SECONDS',/)
```

```
      WRITE(*,298)
298   FORMAT(//,15X,' ENTER 1 TO CONTINUE',//)
      READ(*,*)
C
      RETURN
      END
C
C   SHOW ROUTINE
C
      SUBROUTINE SHOW
      IMPLICIT REAL*8 (A-Z)
      COMMON XAXIS(20),CB(20,20),CG(20,20),CQ(20,20),
     - CO(20,20),CA(20,20),CT(20,20),BKY(20),GY(20),QY(20),
     - QY(20),TY(20),AY(20),C,H,E,SANGLE,FOCAL,DSIZE,
     - RANGE,THETA,RAREA,DTIME
C
      INTEGER II
1900  WRITE(*,2000)
2000  FORMAT(//////////,15X,' E D I T   O P T I O N S')
      WRITE(*,2001)
2001  FORMAT(//,15X,'   1. TARGET DATA',/,15X,
     - '   2. BACKGROUND DATA',/,15X,
     - '   3. GAIN DATA',/,15X,
     - '   4. QUANTUM EFFICIENCY DATA',/,15X,
     - '   5. OPTIC TRANSMISSION DATA',/,15X,
     - '   6. ATMOSHERIC TRANSMISSION DATA',/,15X,
     - '   7. SENSOR DATA',/,15X,
     - '   8. CHANGE WAVELENGTH RANGE',/,15X,
     - '   9. EXIT EDIT',//,15X,
     - '   ENTER DESIRED CHOICE 1-9',////)
      READ(*,*) II
      IF ((II.LT.1).OR.(II.GT.9)) GOTO 1900
      GOTO(2010,2020,2030,2040,2050,2060,2070,
     - 2075,2080),II
2020  CALL DISPLAY(1)
      CALL YESNO(II)
      IF (II.EQ.1) CALL EDIT(1)
      GOTO 1900
2010  CALL DISPLAY(6)
      CALL YESNO(II)
      IF (II.EQ.1) CALL EDIT(6)
      GOTO 1900
2040  CALL DISPLAY(3)
      CALL YESNO(II)
      IF (II.EQ.1) CALL EDIT(3)
      GOTO 1900
2050  CALL DISPLAY(4)
      CALL YESNO(II)
      IF (II.EQ.1) CALL EDIT(4)
      GOTO 1900
2060  CALL DISPLAY(5)
      CALL YESNO(II)
      IF (II.EQ.1) CALL EDIT(5)
      GOTO 1900
2030  CALL DISPLAY(2)
      CALL YESNO(II)
      IF (II.EQ.1) CALL EDIT(2)
      GOTO 1900
2070  CALL TEDIT
      GOTO 1900
2075  CALL XEDIT
      GOTO 1900
2080  RETURN
      END
C
C    YES NO SUBROUTINE
C
      SUBROUTINE YESNO(A)
      INTEGER A
      WRITE(*,*) '   ENTER   1  TO  EDIT, 2  TO  CONTINUE'
      READ(*,*) A
      IF ((A.LT.1).OR.(A.GT.2)) A=2
      RETURN
      END
C
C   EDIT SUBROUTINE   300
C
      SUBROUTINE EDIT(A)
      IMPLICIT REAL*8 (A-Z)
      COMMON XAXIS(20),CB(20,20),CG(20,20),CQ(20,20),
     - CO(20,20),CA(20,20),CT(20,20),BKY(20),GY(20),QY(20),
     - QY(20),TY(20),AY(20),C,H,E,SANGLE,FOCAL,DSIZE,
     - RANGE,THETA,RAREA,DTIME

      INTEGER A,K
305   WRITE(*,310)
310   FORMAT(1X,' ENTER 1-20 FOR EDIT, 0 TO EXIT, 21 TO',
     - ' REDISPLAY ')
      READ(*,*) K
      IF ((K.LT.0).OR.(K.GT.21)) GOTO 305
      IF (K.EQ.0) GOTO 390
      IF (K.EQ.21) THEN
         CALL DISPLAY(A)
         GOTO 305
      END IF
      WRITE(*,315) XAXIS(K)
315   FORMAT(/,' ENTER DATA (D16.8) FOR ',D8.3,' METERS')
320   FORMAT(D16.8)
      GOTO(330,335,340,345,350,355),A
330   READ(*,320) BKY(K)
      GOTO 305
335   READ(*,320) GY(K)
      GOTO 305
340   READ(*,320) QY(K)
```

```
      GOTO 305
345   READ(*,320) OY(K)
      GOTO 305
350   READ(*,320) AY(K)
      GOTO 305
355   READ(*,320) TY(K)
      GOTO 305
390   RETURN
      END
C
C  EDIT XAXIS
C
      SUBROUTINE XEDIT
      IMPLICIT REAL*8 (A-Z)
      COMMON XAXIS(20),CB(20,20),CG(20,20),CQ(20,20),
     - CO(20,20),CA(20,20),CT(20,20),BKY(20),GY(20),QY(20),
     - OY(20),TY(20),AY(20),C,H,E,SANGLE,FOCAL,DSIZE,
     - RANGE,THETA,RAREA,DTIME
 C
      INTEGER I
      REAL A1,B1
      WRITE(*,500)
500   FORMAT(//,15X,'** EDIT ROUTINE FOR WAVELENGTHS **',
     - //,15X,'ENTER LOWER WAVELENGTH BOUND IN METERS',
     - ' (REAL)')
      READ(*,*) A1
      XAXIS(1)=DBLE(A1)
      WRITE(*,510)
510   FORMAT(/,15X,'ENTER WAVELENGTH INTERVAL (REAL)')
      READ(*,*) B1
      DO 520 I=2,20
      XAXIS(I)=XAXIS(I-1)+DBLE(B1)
520   CONTINUE
      RETURN
      END
C
C   TEDIT
C
      SUBROUTINE TEDIT
      IMPLICIT REAL*8 (A-Z)
      COMMON XAXIS(20),CB(20,20),CG(20,20),CQ(20,20),
     - CO(20,20),CA(20,20),CT(20,20),BKY(20),GY(20),QY(20),
     - OY(20),TY(20),AY(20),C,H,E,SANGLE,FOCAL,DSIZE,
     - RANGE,THETA,RAREA,DTIME
C
      REAL*8 HLP
      INTEGER II
285   FORMAT(//,15X,'  FOCAL LENGTH = ',D20.11,
     - '  METERS',/)
287   FORMAT(//,15X,' DETECTOR SIZE = ',D20.11,
     - '  METERS',/)
289   FORMAT(//,15X,'  TARGET RANGE = ',D20.11,
     - '  METERS',/)
291   FORMAT(//,15X,'          THETA = ',D20.11,
     - '  RADIANS',/)
293   FORMAT(//,15X,' RECEIVER AREA = ',D20.11,
     - '  METERS SQR',/)
297   FORMAT(//,15X,'    DWELL TIME = ',D20.11,
     - '  SECONDS',/)
      WRITE(*,285) FOCAL
      CALL YESNO(I1)
      IF (I1.EQ.1) CALL THELP(FOCAL)
      WRITE(*,287) DSIZE
      CALL YESNO(I1)
      IF (I1.EQ.1) CALL THELP(DSIZE)
      WRITE(*,289) RANGE
      CALL YESNO(I1)
      IF (I1.EQ.1) CALL THELP(RANGE)
      WRITE(*,291) THETA
      CALL YESNO(I1)
      IF (I1.EQ.1) CALL THELP(THETA)
      WRITE(*,293) RAREA
      CALL YESNO(I1)
      IF (I1.EQ.1) CALL THELP(RAREA)
      WRITE(*,297) DTIME
      CALL YESNO(I1)
      IF (I1.EQ.1) CALL THELP(DTIME)
      HLP=DSIZE/FOCAL
      SANGLE=3.1415927D0*2*(1-DCOS(DATAN(HLP)))
      RETURN
      END
C
C  THELP
C
      SUBROUTINE THELP(A)
      REAL*8 A
      WRITE(*,*) '              ENTER NEW VALUE (D16.8) '
      READ(*,*) A
      RETURN
      END
C
C   DISPLAY ROUTINE  200
C
      SUBROUTINE DISPLAY(K)
      IMPLICIT REAL*8 (A-Z)
      COMMON XAXIS(20),CB(20,20),CG(20,20),CQ(20,20),
     - CO(20,20),CA(20,20),CT(20,20),BKY(20),GY(20),QY(20),
     - OY(20),TY(20),AY(20),C,H,E,SANGLE,FOCAL,DSIZE,
     - RANGE,THETA,RAREA,DTIME
C
      INTEGER K,I,J
      GOTO(202,204,206,208,210,231),K
202   WRITE(*,201)
      GOTO 220
```

```
204     WRITE(*,203)
        GOTO 220
206     WRITE(*,205)
        GOTO 220
208     WRITE(*,207)
        GOTO 220
210     WRITE(*,211)
        GOTO 220
231     WRITE(*,209)
201     FORMAT(1X,////,' ** BACKGROUND RADIANCE DATA **')
203     FORMAT(1X,///,' ** GAIN DATA **')
205     FORMAT(1X,///,' ** QUANTUM EFFICIENCY DATA **')
207     FORMAT(1X,///,' ** OPTIC TRANSMISSION DATA **')
209     FORMAT(1X,///,' ** TARGET INTENSITY DATA **')
211     FORMAT(1X,///,' ** ATMOSHERIC TRANSMISSION DATA **')
C
220     GOTO(222,224,226,228,232,234),K
222     WRITE(*,212)
        GOTO 230
224     WRITE(*,213)
        GOTO 230
226     WRITE(*,215)
        GOTO 230
228     WRITE(*,216)
        GOTO 230
232     WRITE(*,219)
        GOTO 230
234     WRITE(*,217)
212     FORMAT(1X,'   WAVELENGTH(METERS)          ',
     - ' WATTS/M2-SR')
213     FORMAT(1X,'   WAVELENGTH(METERS)          GAIN')
215     FORMAT(1X,'   WAVELENGTH(METERS)          ',
     - 'QUANTUM EFF')
216     FORMAT(1X,'   WAVELENGTH(METERS)          VALUE')
217     FORMAT(1X,'   WAVELENGTH(METERS)          ',
     - ' WATTS/STER')
219     FORMAT(1X,'   WAVELENGTH(METERS)          PERCENT')
C
230     DO 250 I=1,20
        GOTO(330,335,340,345,350,355),K
330     WRITE(*,240) I,XAXIS(I),BKY(I)
        GOTO 250
335     WRITE(*,240) I,XAXIS(I),GY(I)
        GOTO 250
340     WRITE(*,240) I,XAXIS(I),QY(I)
        GOTO 250
345     WRITE(*,240) I,XAXIS(I),OY(I)
        GOTO 250
350     WRITE(*,240) I,XAXIS(I),AY(I)
        GOTO 250
355     WRITE(*,240) I,XAXIS(I),TY(I)
240     FORMAT(1X,' ',I2,'.  ',D8.3,'          ',D20.11)
250     CONTINUE
        WRITE(*,255)
255     FORMAT(1X,' ********************************',
     -  '**********')
        RETURN
        END
C
C   LOAD DATA
C
        SUBROUTINE LOADATA
        IMPLICIT REAL*8 (A-Z)
        COMMON XAXIS(20),CB(20,20),CG(20,20),CQ(20,20),
     -  CO(20,20),CA(20,20),CT(20,20),BKY(20),GY(20),QY(20),
     -  OY(20),TY(20),AY(20),C,H,E,SANGLE,FOCAL,DSIZE,
     -  RANGE,THETA,RAREA,DTIME
C
        REAL*8 HLP
        INTEGER I
        REWIND(1)
        WRITE(*,200)
200     FORMAT(///,20X,'  LOADING DATA',///)
C
C   X AXIS
C
        DO 1040 I=1,20
        READ(1,*) XAXIS(I)
1040    CONTINUE
C
C       BACKGROUND
C
        DO 1050 I=1,20
        READ(1,*) BKY(I)
1050    CONTINUE
C
C   GAIN  DATA
C
        DO 1100 I=1,20
        READ(1,*) GY(I)
1100    CONTINUE
C
C   QUANTUM EFFICIENCY DATA
C
        DO 1150 I=1,20
        READ(1,*) QY(I)
1150    CONTINUE
C
C    OPTIC TRANSMISSION DATA
C
        DO 1200 I=1,20
        READ(1,*) OY(I)
1200    CONTINUE
C
```

```
C  TARGET
C
        DO 1250 I=1,20
        READ(1,*) TY(I)
1250    CONTINUE
C
C  ATMOSPHERE
C
        DO 1280 I=1,20
        READ(1,*) AY(I)
1280    CONTINUE
C
C
C OTHER DATA
C
        E=1.602D-19
        H=6.626D-34
        C=2.998D+8
        READ(1,*) DTIME
        READ(1,*) FOCAL
        READ(1,*) DSIZE
        READ(1,*) RANGE
        READ(1,*) THETA
        READ(1,*) RAREA
        HLP=DSIZE/FOCAL
        SANGLE=3.1415927D0*2*(1-DCOS(DATAN(HLP)))
        RETURN
        END
C
C  SAVE SUBROUTINE
C
        SUBROUTINE SAVES
        IMPLICIT REAL*8 (A-Z)
        COMMON XAXIS(20),CB(20,20),CG(20,20),CO(20,20),
     -  CO(20,20),CA(20,20),CT(20,20),BKY(20),GY(20),QY(20),
     -  OY(20),TY(20),AY(20),C,H,E,SANGLE,FOCAL,DSIZE,
     -  RANGE,THETA,RAREA,DTIME
C
        INTEGER I
        REWIND 1
        DO 1250 I=1,20
        WRITE(1,*) XAXIS(I)
1250    CONTINUE
        DO 1300 I=1,20
        WRITE(1,*) BKY(I)
1300    CONTINUE
        DO 1350 I=1,20
        WRITE(1,*) GY(I)
1350    CONTINUE
        DO 1400 I=1,20
        WRITE(1,*) QY(I)
1400    CONTINUE
        DO 1450 I=1,20
        WRITE(1,*) OY(I)
1450    CONTINUE
        DO 1500 I=1,20
        WRITE(1,*) TY(I)
1500    CONTINUE
        DO 1550 I=1,20
        WRITE(1,*) AY(I)
1550    CONTINUE
C
        WRITE(1,*) DTIME
        WRITE(1,*) FOCAL
        WRITE(1,*) DSIZE
        WRITE(1,*) RANGE
        WRITE(1,*) THETA
        WRITE(1,*) RAREA
        WRITE(*,1600)
1600    FORMAT(///,15X,'CURRENT PARAMETERS SAVED',///////)
C
        RETURN
        END
C
C   WRITE DATA TO FILE 6
C
        SUBROUTINE PRNTIT(A,B,IB,IT,SN,ERR)
        IMPLICIT REAL*8 (A-Z)
        COMMON XAXIS(20),CB(20,20),CG(20,20),CO(20,20),
     -  CO(20,20),CA(20,20),CT(20,20),BKY(20),GY(20),QY(20),
     -  OY(20),TY(20),AY(20),C,H,E,SANGLE,FOCAL,DSIZE,
     -  RANGE,THETA,RAREA,DTIME

        REAL*8 A,B,IB,IT,SN,ERR
        INTEGER I
        REWIND 6
C
        WRITE(6,260)
260     FORMAT(1X,///,'      *********      DATA FOR',
     -  ' APPROXIMATING',
     -        ' FUNCTIONS      **********',//)
        WRITE(6,265)
265     FORMAT(1X,'WAVELTH      TARGET      BACKGRD      GAIN',
     -  '     QNTEFF      OPTICS     ATMOSPHR',/,' METERS      ',
     -  ' W/ST        W/M2-S       VALUE       VALUE       ',
     -  'PERCENT    PERCENT',/)
        DO 275 I=1,20
        WRITE(6,270) XAXIS(I),TY(I),BKY(I),GY(I),QY(I),
     -              OY(I),AY(I)
270     FORMAT(1X,D9.4,2X,D8.3,3X,D8.3,4X,D8.3,2X,D8.3,2X,
     -  D8.3,3X,D8.3)
275     CONTINUE
C
        WRITE(6,282)
```

```
282     FORMAT(//,20X,'*****   SENSOR DATA   *****',//)
        WRITE(6,285) FOCAL
        WRITE(6,287) DSIZE
        WRITE(6,289) RANGE
        WRITE(6,291) THETA
        WRITE(6,293) RAREA
        WRITE(6,295) SANGLE
        WRITE(6,297) DTIME
285     FORMAT('  FOCAL LENGTH = ',D20.11,'  METERS')
287     FORMAT(' DETECTOR SIZE = ',D20.11,'  METERS')
289     FORMAT('  TARGET RANGE = ',D20.11,'  METERS')
291     FORMAT('         THETA = ',D20.11,'  RADIANS')
293     FORMAT(' RECEIVER AREA = ',D20.11,'  METERS SQR')
295     FORMAT(' REC SOLID ANG = ',D20.11,'  STER')
297     FORMAT('    DWELL TIME = ',D20.11,'  SECONDS',/)
        WRITE(6,900) A,B
900     FORMAT(//,'  INTEGRATION LIMITS -> ',D20.11,/,
     -                                    TO ',D20.11,/)
        WRITE(6,910) IB,IT
910     FORMAT(' **************  RESULTS  ****************',/,
     -  ' *** CURRENTS ***',/,'  BACKGROUND - ',D20.11,/,
     -                '       TARGET - ',D20.11,/)
        IB=IB/E
        IT=IT/E
        WRITE(6,912) IB,IT
912     FORMAT(' *** PHOTON COUNTS ***',/,'  BACKGROUND - ',
     -  D20.11,/,'       TARGET - ',D20.11)
        WRITE(6,915) SN,ERR
915     FORMAT(// '  SIGNAL TO NOISE IS ->> ',D20.11,//,
     -                '     ESTIMATED ERROR - ',D10.5)
        RETURN
        END
C
        SUBROUTINE DTABLE(ERROR)
        IMPLICIT REAL*8 (A-Z)
        COMMON XAXIS(20),CB(20,20),CG(20,20),CQ(20,20),
     -  CO(20,20),CA(20,20),CT(20,20),BKY(20),GY(20),QY(20),
     -  OY(20),TY(20),AY(20),C,H,E,SANGLE,FOCAL,DSIZE,
     -  RANGE,THETA,RAREA,DTIME
C
        INTEGER ERROR,N,M,NM1,ISUB,I,J
C
C CHECK FOR ARGUMENT CONSISTENCY
C
        WRITE(*,20)
20      FORMAT(////////,10X,
     -  ' CALCULATING DIVIDED DIFFERENCE TABLES ',////////)
        N=20
        M=19
        NM1=N-1
        DO 3 I=1,NM1
        CB(I,1)=(BKY(I+1)-BKY(I))/(XAXIS(I+1)-XAXIS(I))
        CG(I,1)=(GY(I+1)-GY(I))/(XAXIS(I+1)-XAXIS(I))
        CQ(I,1)=(QY(I+1)-QY(I))/(XAXIS(I+1)-XAXIS(I))
        CO(I,1)=(OY(I+1)-OY(I))/(XAXIS(I+1)-XAXIS(I))
        CT(I,1)=(TY(I+1)-TY(I))/(XAXIS(I+1)-XAXIS(I))
        CA(I,1)=(AY(I+1)-AY(I))/(XAXIS(I+1)-XAXIS(I))
3       CONTINUE
C
        DO 5 J=2,M
        DO 5 I=J,NM1
        ISUB=I+1-J
        CB(I,J) = (CB(I,J-1)-CB(I-1,J-1))/
     -            (XAXIS(I+1)-XAXIS(ISUB))
        CG(I,J) = (CG(I,J-1)-CG(I-1,J-1))/
     -            (XAXIS(I+1)-XAXIS(ISUB))
        CQ(I,J) = (CQ(I,J-1)-CQ(I-1,J-1))/
     -            (XAXIS(I+1)-XAXIS(ISUB))
        CO(I,J) = (CO(I,J-1)-CO(I-1,J-1))/
     -            (XAXIS(I+1)-XAXIS(ISUB))
        CT(I,J) = (CT(I,J-1)-CT(I-1,J-1))/
     -            (XAXIS(I+1)-XAXIS(ISUB))
        CA(I,J) = (CA(I,J-1)-CA(I-1,J-1))/
     -            (XAXIS(I+1)-XAXIS(ISUB))
5       CONTINUE
C
        ERROR=0
        RETURN
        END
C
        REAL*8 FUNCTION FNEWT(MODE,XARG,ERROR)
        IMPLICIT REAL*8 (A-Z)
        COMMON XAXIS(20),CB(20,20),CG(20,20),CQ(20,20),
     -  CO(20,20),CA(20,20),CT(20,20),BKY(20),GY(20),QY(20),
     -  OY(20),TY(20),AY(20),C,H,E,SANGLE,FOCAL,DSIZE,
     -  RANGE,THETA,RAREA,DTIME
C
        REAL*8 XARG,YEST,HELPER
        INTEGER MODE,N,M,IDEG,ERROR,K,I,MAX,ISUB1,
     -  ISUB2,IDEGM1
C
C
        N=20
        M=19
        IDEG=18
C
        DO 4 I=1,N
        IF ((I.EQ.N).OR.(XARG.LE.XAXIS(I))) GOTO 5
4       CONTINUE
5       MAX=I+IDEG/2
C
        IF (MAX.LE.IDEG) MAX=IDEG+1
        IF (MAX.GT.N) MAX=N
C
```

```
C COMPUTE VALUE
C
      GOTO(20,25,30,35,40,45),MODE
20    YEST=CB(MAX-1,IDEG)
      GOTO 60
25    YEST=CG(MAX-1,IDEG)
      GOTO 60
30    YEST=CO(MAX-1,IDEG)
      GOTO 60
35    YEST=CO(MAX-1,IDEG)
      GOTO 60
40    YEST=CT(MAX-1,IDEG)
      GOTO 60
45    YEST=CA(MAX-1,IDEG)
60    IDEGM1=IDEG-1
      DO 12 I=1,IDEGM1
      ISUB1=MAX-I
      ISUB2=IDEG-I
      GOTO(70,75,80,85,90,95),MODE
70    YEST=YEST*(XARG-XAXIS(ISUB1))*CB(ISUB1-1,ISUB2)
      GOTO 12
75    YEST=YEST*(XARG-XAXIS(ISUB1))*CG(ISUB1-1,ISUB2)
      GOTO 12
80    YEST=YEST*(XARG-XAXIS(ISUB1))*CO(ISUB1-1,ISUB2)
      GOTO 12
85    YEST=YEST*(XARG-XAXIS(ISUB1))*CO(ISUB1-1,ISUB2)
      GOTO 12
90    YEST=YEST*(XARG-XAXIS(ISUB1))*CT(ISUB1-1,ISUB2)
      GOTO 12
95    YEST=YEST*(XARG-XAXIS(ISUB1))*CA(ISUB1-1,ISUB2)
12    CONTINUE
13    ISUB1=MAX-IDEG
      ERROP=0
      GOTO(100,105,110,115,120,125),MODE
100   FNEWT=YEST*(XARG-XAXIS(ISUB1))*BKY(ISUB1)
      GOTO 200
105   FNEWT=YEST*(XARG-XAXIS(ISUB1))*GY(ISUB1)
      GOTO 200
110   FNEWT=YEST*(XARG-XAXIS(ISUB1))*QY(ISUB1)
      GOTO 200
115   FNEWT=YEST*(XARG-XAXIS(ISUB1))*OY(ISUB1)
      GOTO 200
120   FNEWT=YEST*(XARG-XAXIS(ISUB1))*TY(ISUB1)
      GOTO 200
125   FNEWT=YEST*(XARG-XAXIS(ISUB1))*AY(ISUB1)
200   RETURN
      END
```

Appendix B

LOWTRAN RESULTS

This appendix contains an abbreviated listing of the results from the computer runs using the LOWTRAN 6 code. The data is arranged in order of decreasing path length starting with a path length of 90 km representing a path from 10 km to space. For each path length, transmission values are given as a function of wavelength for the various contributors to ultraviolet attenuation, ozone, molecular scattering and aerosol scattering. Also given is the total transmission at each wavelength as well as an total transmission averaged over wavelength.

SUMMARY OF THE GEOMETRY CALCULATION

H1	=	10.000 KM
H2	=	100.000 KM
ANGLE	=	.000 DEG
RANGE	=	90.000 KM
BETA	=	.000 DEG
PHI	=	180.000 DEG
HMIN	=	10.000 KM
BENDING	=	.000 DEG
LEN	=	0

WAVELENGTH MICRONS	TOTAL TRANS	OZONE TRANS	MOL SCAT TRANS	AEROSOL TRANS
.313	.4055	.5376	.7636	.9878
.301	.0417	.0579	.7293	.9878
.291	.0000	.0000	.6922	.9878
.281	.0000	.0000	.6527	.9878
.272	.0000	.0000	.6108	.9878
.263	.0000	.0000	.5669	.9878
.255	.0000	.0000	.5215	.9878
.248	.0000	.0000	.4750	.9878
.240	.0000	.0000	.4279	.9878
.234	.0000	.0000	.3809	.9879
.227	.0000	.0000	.3346	.9879
.221	.0000	.0000	.2897	.9879
.216	.0000	.0002	.2468	.9879
.210	.0000	.0086	.2066	.9879
.205	.0000	.0521	.1696	.9879
.200	.0000	.0647	.1363	.9879

AVERAGE TRANSMITTANCE = .0163

SUMMARY OF THE GEOMETRY CALCULATION

H1	=	20.000 KM
H2	=	100.000 KM
ANGLE	=	.000 DEG
RANGE	=	80.000 KM
BETA	=	.000 DEG
PHI	=	180.000 DEG
HMIN	=	20.000 KM
BENDING	=	.000 DEG
LEN	=	0

WAVELENGTH MICRONS	TOTAL TRANS	OZONE TRANS	MOL SCAT TRANS	AEROSOL TRANS
.313	.6233	.6618	.9451	.9964
.301	.1403	.1504	.9360	.9964
.291	.0007	.0008	.9259	.9964
.281	.0000	.0000	.9145	.9964
.272	.0000	.0000	.9019	.9964
.263	.0000	.0000	.8880	.9965
.255	.0000	.0000	.8726	.9965
.248	.0000	.0000	.8557	.9965
.240	.0000	.0000	.8372	.9965
.234	.0000	.0000	.8170	.9965
.227	.0000	.0000	.7951	.9965
.221	.0000	.0000	.7715	.9965
.216	.0006	.0032	.7460	.9965
.210	.0058	.0422	.7188	.9965
.205	.0151	.1403	.6897	.9965
.200	.0148	.1620	.6588	.9966

AVERAGE TRANSMITTANCE = .0321

SUMMARY OF THE GEOMETRY CALCULATION

H1	=	30.000 KM
H2	=	100.000 KM
ANGLE	=	.000 DEG
RANGE	=	70.000 KM
BETA	=	.000 DEG
PHI	=	180.000 DEG
HMIN	=	30.000 KM
BENDING	=	.000 DEG
LEN	=	0

WAVELENGTH MICRONS	TOTAL TRANS	OZONE TRANS	MOL SCAT TRANS	AEROSOL TRANS
.313	.8736	.8847	.9878	.9997
.301	.5615	.5698	.9858	.9997
.291	.1178	.1198	.9834	.9997
.281	.0028	.0029	.9808	.9997
.272	.0000	.0000	.9778	.9997
.263	.0000	.0000	.9745	.9997
.255	.0000	.0000	.9708	.9997
.248	.0000	.0000	.9667	.9997
.240	.0000	.0000	.9622	.9997
.234	.0001	.0001	.9571	.9997
.227	.0018	.0022	.9515	.9997
.221	.0242	.0321	.9452	.9997
.216	.1279	.1823	.9384	.9997
.210	.2563	.3906	.9308	.9997
.205	.3472	.5581	.9225	.9997
.200	.3497	.5825	.9134	.9997

AVERAGE TRANSMITTANCE = .1367

SUMMARY OF THE GEOMETRY CALCULATION

H1	=	40.000 KM
H2	=	100.000 KM
ANGLE	=	.000 DEG
RANGE	=	60.000 KM
BETA	=	.000 DEG
PHI	=	180.000 DEG
HMIN	=	40.000 KM
BENDING	=	.000 DEG
LEN	=	0

WAVELENGTH MICRONS	TOTAL TRANS	OZONE TRANS	MOL SCAT TRANS	AEROSOL TRANS
.313	.9775	.9805	.9971	.9999
.301	.9102	.9134	.9966	.9999
.291	.7078	.7107	.9960	.9999
.281	.3877	.3895	.9953	.9999
.272	.1442	.1451	.9946	.9999
.263	.0639	.0645	.9938	.9999
.255	.0464	.0469	.9929	.9999
.248	.0576	.0586	.9919	.9999
.240	.1053	.1080	.9908	.9999
.234	.2037	.2114	.9895	.9999
.227	.3543	.3729	.9881	.9999
.221	.5372	.5747	.9866	.9999
.216	.6984	.7604	.9848	.9999
.210	.7771	.8595	.9829	.9999
.205	.8126	.9104	.9808	.9999
.200	.8113	.9167	.9785	.9999

AVERAGE TRANSMITTANCE = .4467

SUMMARY OF THE GEOMETRY CALCULATION

H1	=	50.000 KM
H2	=	100.000 KM
ANGLE	=	.000 DEG
RANGE	=	50.000 KM
BETA	=	.000 DEG
PHI	=	180.000 DEG
HMIN	=	50.000 KM
BENDING	=	.000 DEG
LEN	=	0

WAVELENGTH MICRONS	TOTAL TRANS	OZONE TRANS	MOL SCAT TRANS	AEROSOL TRANS
.313	.9973	.9981	.9992	1.0000
.301	.9904	.9914	.9991	1.0000
.291	.9668	.9679	.9989	1.0000
.281	.9126	.9138	.9987	1.0000
.272	.8300	.8315	.9985	1.0000
.263	.7677	.7694	.9983	1.0000
.255	.7440	.7464	.9981	1.0000
.248	.7588	.7625	.9978	1.0000
.240	.8027	.8083	.9975	1.0000
.234	.8533	.8619	.9871	1.0000
.227	.8973	.9100	.9867	1.0000
.221	.9310	.9484	.9863	1.0000
.216	.9517	.9741	.9858	1.0000
.210	.9588	.9856	.9853	1.0000
.205	.9607	.9911	.9847	1.0000
.200	.9591	.9917	.9740	1.0000

AVERAGE TRANSMITTANCE = .8869

SUMMARY OF THE GEOMETRY CALCULATION

H1	=	60.000 KM
H2	=	100.000 KM
ANGLE	=	.000 DEG
RANGE	=	40.000 KM
BETA	=	.000 DEG
PHI	=	180.000 DEG
HMIN	=	60.000 KM
BENDING	=	.000 DEG
LEN	=	0

WAVELENGTH MICRONS	TOTAL TRANS	OZONE TRANS	MOL SCAT TRANS	AEROSOL TRANS
.313	.9995	.9997	.9998	1.0000
.301	.9985	.9988	.9997	1.0000
.291	.9951	.9954	.9997	1.0000
.281	.9869	.9873	.9996	1.0000
.272	.9736	.9741	.9996	1.0000
.263	.9628	.9634	.9995	1.0000
.255	.9584	.9593	.9995	1.0000
.248	.9609	.9622	.9994	1.0000
.240	.9683	.9702	.9993	1.0000
.234	.9764	.9791	.9992	1.0000
.227	.9829	.9867	.9991	1.0000
.221	.9875	.9925	.9990	1.0000
.216	.9900	.9963	.9989	1.0000
.210	.9904	.9979	.9987	1.0000
.205	.9902	.9987	.9985	1.0000
.200	.9897	.9988	.9984	1.0000

AVERAGE TRANSMITTANCE = .9811

SUMMARY OF THE GEOMETRY CALCULATION

H1	=	70.000 KM
H2	=	100.000 KM
ANGLE	=	.000 DEG
RANGE	=	30.000 KM
BETA	=	.000 DEG
PHI	=	180.000 DEG
HMIN	=	70.000 KM
BENDING	=	.000 DEG
LEN	=	0

WAVELENGTH MICRONS	TOTAL TRANS	OZONE TRANS	MOL SCAT TRANS	AEROSOL TRANS
.313	.9999	1.0000	.9999	1.0000
.301	.9998	.9999	.9999	1.0000
.291	.9994	.9995	.9999	1.0000
.281	.9984	.9985	.9999	1.0000
.272	.9969	.9970	.9999	1.0000
.263	.9956	.9957	.9999	1.0000
.255	.9950	.9952	.9999	1.0000
.248	.9953	.9956	.9999	1.0000
.240	.9961	.9965	.9998	1.0000
.234	.9969	.9976	.9998	1.0000
.227	.9976	.9985	.9998	1.0000
.221	.9980	.9991	.9998	1.0000
.216	.9981	.9996	.9997	1.0000
.210	.9980	.9998	.9997	1.0000
.205	.9979	.9999	.9997	1.0000
.200	.9978	.9999	.9996	1.0000

AVERAGE TRANSMITTANCE = .9975

SUMMARY OF THE GEOMETRY CALCULATION

H1	=	80.000 KM
H2	=	100.000 KM
ANGLE	=	.000 DEG
RANGE	=	20.000 KM
BETA	=	.000 DEG
PHI	=	180.000 DEG
HMIN	=	80.000 KM
BENDING	=	.000 DEG
LEN	=	0

WAVELENGTH MICRONS	TOTAL TRANS	OZONE TRANS	MOL SCAT TRANS	AEROSOL TRANS
.313	1.0000	1.0000	1.0000	1.0000
.301	1.0000	1.0000	1.0000	1.0000
.291	.9999	1.0000	1.0000	1.0000
.281	.9999	.9999	1.0000	1.0000
.272	.9997	.9998	1.0000	1.0000
.263	.9996	.9997	1.0000	1.0000
.255	.9996	.9996	1.0000	1.0000
.248	.9996	.9996	1.0000	1.0000
.240	.9996	.9997	1.0000	1.0000
.234	.9997	.9998	1.0000	1.0000
.227	.9997	.9999	1.0000	1.0000
.221	.9997	.9999	1.0000	1.0000
.216	.9997	1.0000	1.0000	1.0000
.210	.9997	1.0000	.9999	1.0000
.205	.9997	1.0000	.9999	1.0000
.200	.9996	1.0000	.9999	1.0000

AVERAGE TRANSMITTANCE = .9997

SUMMARY OF THE GEOMETRY CALCULATION

H1	=	90.000 KM
H2	=	100.000 KM
ANGLE	=	.000 DEG
RANGE	=	10.000 KM
BETA	=	.000 DEG
PHI	=	180.000 DEG
HMIN	=	90.000 KM
BENDING	=	.000 DEG
LEN	=	0

WAVELENGTH MICRONS	TOTAL TRANS	OZONE TRANS	MOL SCAT TRANS	AEROSOL TRANS
.313	1.0000	1.0000	1.0000	1.0000
.301	1.0000	1.0000	1.0000	1.0000
.291	1.0000	1.0000	1.0000	1.0000
.281	1.0000	1.0000	1.0000	1.0000
.272	1.0000	1.0000	1.0000	1.0000
.263	1.0000	1.0000	1.0000	1.0000
.255	1.0000	1.0000	1.0000	1.0000
.248	1.0000	1.0000	1.0000	1.0000
.240	1.0000	1.0000	1.0000	1.0000
.234	1.0000	1.0000	1.0000	1.0000
.227	1.0000	1.0000	1.0000	1.0000
.221	1.0000	1.0000	1.0000	1.0000
.216	1.0000	1.0000	1.0000	1.0000
.210	1.0000	1.0000	1.0000	1.0000
.205	.9999	1.0000	1.0000	1.0000
.200	.9999	1.0000	1.0000	1.0000

AVERAGE TRANSMITTANCE = .9997

Bibliography

Abell, G.O. Exploration of the Universe. New York: Holt, Rinehart and Winston, 1975.

Band, H.E. and Block, L.C. "Spectral Radiance Measurements of the Earth from High Altitudes," Applied Optics, 6: 355-358 (March 1965).

Blouke, M.M. and others. "800 x 800 charge-coupled device image sensor," Optical Engineering, 22: 607-613 (October 1983).

------. "Ultraviolet downconverting phosphor for use with silicon CCD imagers," Applied Optics, 19: 3318-3321 (October 1980).

Bonds, R. The Soviet War Machine. London: Salamander Book Ltd., 1976.

Camac, M. and Sepucha, R.C. "Analysis of Ultraviolet signature from Tactical Missile Rocket Exhaust Plumes," 9th JANNAF Plume Technology Conference, 347-378. Redstone Arsenal Alabama, Feb 1976. (AD-C009 411 Secret Report)

Carruthers G.R. and Page, T. "Apollo 16 Far-UV Camera/ Spectrograph: Earth Observations," Science. 177: 788-791 (1972).

Carter, A.B. Directed Energy Missile Defense in Space. Prepared under contract for the Office of Technology Assessment, Washington, April 1984.

Coleman, C.I. "Imaging detectors for the ultraviolet," Applied Optics, 20: 3693-3703 (November 1981).

Daugherty, T.L. and others. UV and IR Radiation from IUS SRM-II Plume. Arnold Engineering Development Center, Arnold AFS Tenn., Jan 1986 (AD-C038 159 Secret Report)

Davies, J.G. "The Titan Launch Vehicle Family," Spaceflight, 25: 36-38 (January 1983).

Dorian, M. and Harshbarger, F. "Measurement of the Atmospheric Spectral Radiance at 35 km in the Near Ultraviolet," Applied Optics, 6: 1487-1491 (September 1967)

Good, Robert E. UV Observations of High Altitude Missile Plumes. AFGL-TR-76-0192. AF Geophysics Lab, Hanscom AFB Mass., August 1976. (AD-C008 994)

Green, A.E.S. and Barth, C.A. "Calculations of the Photoelectron Excitation of the Dayglow," Journal of Geophysical Research, 72. 3975-3983 (August 1967)

Green, A.E.S. The Middle Ultraviolet: Its Science and Technology. New York: John Wiley & Sons, Inc., 1966.

Gross, J.S. and Montague, J.E. Data processing for Advanced Midcourse Optical Sensors: Vol 5. Contract DASG60-77-C-0025. Honeywell Systems and Research Center, Minneapolis Minn., Jan 1978. (AD-C013 392 Secret Report)

Hines, C.O. and others. Physics of the Earth's Upper Atmosphere. Englewood Cliffs, New Jersey: Prentice-Hall, Inc., 1965.

Huffman, R.E. Private communication regarding the spatial distribution of the earths UV airglow. AF Geophysics Laboratory, Hanscom AFB Mass., 1986.

Jacobs, T.A. and others. Measurements of Ultraviolet Emission from Rocket Exhaust Plumes with in situ Determined Atmospheric Corrections. Contract AF04695-469. The Aerospace Corporation, El Segundo CA., September 1965.

Kingston, R.H. Detection of Optical and Infrared Radiation. New York: Springer-Verlag. 1979.

Kneizys, F.X. and others. Atmospheric Transmittance/ Radiance: Computer Code LOWTRAN 6. AFGL-TR-83-0187. AF Geophysics Laboratory, Hanscom AFB Mass., August 1983.

Lyons, R.B. and others. "Calculation of Visible Radiation from Missile Plumes," AIAA 16th Thermophysics Conference. Paper No AIAA-81-1111. AIAA Press, New York, June 1981.

McCormac, B.M. Aurora and Airglow. New York: Reinhold Publishing Corporation, 1967.

McGregor, W.K. and others. Summary of the PAM DII Plume UV Radiation Measurements at Simulated Altitudes. Arnold Engineering Development Center, Arnold AFS Tenn., Sept 1985 (AD-C038 285 Secret Report).

McIntyre, A. and others. MSMP TEM-2 IR and UV Radiation Data Analysis. AFGL-TR-81-0118. Air Force Geophysics Lab, Hanscom AFB Mass., Jan 1981. (AD-C025 511 Secret Report)

Pauw, H. "New Insights Into Space Activities," Spaceflight, 28: 250-251 (June 1986).

Reitz, Larry. Private communications regarding the status of ongoing contractual efforts. AF Wright Aeronautical Laboratories, Wright-Patterson AFB, Ohio, 1986.

Roble, R.G. "Chemistry in the Thermosphere and Ionosphere," Chemical & Engineering News, 64: 23-38 (June 16, 1986).

Sears and others. University Physics. Reading, Mass: Addison-Wesley Publishing Co., 1982.

Shackleford, W.L. "Measurements of Ultraviolet Emission from Rocket Plumes ," 15th JANNAF Plume Technology Meeting, 275-283. CPIA Publication 426, Laurel MD, May 1985 (AD-B096 705).

Simmons, F.S. UV Properties of Rockets-Review and Commentary. Contract F04701-35-C-0086. The Aerospace Corporation, El Segundo CA, Feb 1986. (Secret Report)

Slack, Michael and others. UV Mechanisms and Plume Signature Assessment. Contract F40600-80-C-0070. Grumman Aerospace Corporation, Bethpage NY, June 1983. (AD-C031 630 Secret Report).

Slater, P.N. Remote Sensing, Optics and Optical Systems. Reading, Massachusetts: Addison-Wesley Publishing Company, 1980.

Soviet Military Power, 5th Edition. Washington: Government Printing Office, 1986

Air University. Space Handbook. Maxwell AFB: AU Press, 1985

Stergis, C.C. and others. "Ultraviolet Measurements from Titan II Engines," 15th JANNAF Plume Technology Meeting, 53-56. CPIA Publication 426, Laurel MD, May 1985 (AD-B096 705).

Sutton, G.P. and Ross, D.M. Rocket Propulsion Elements. New York: John Wiley & Sons, 1976.

Timothy, J.G. "Multianode microchannel array detector systems: performance characteristics," Optical Engineering, 24: 1066-1071 (November/December 1985).

Validya, D.B. and others. "Remote temperature measurements in gas and gas-coal flames using the OH(0,0) middle-UV band," Applied Optics, 21: 3357-3362 (September 1982).

Viehmann, W. and others. "Ultraviolet sensitive phosphors for silicon imaging detectors," Ultraviolet and Vacuum Ultraviolet System, Proc. SPIE 279: 146-152 (1981).

Waters, C.R. and Fishburne, E.S. "Measurements of the Earth's Airglow in the Vacuum Ultraviolet," The Scientific Results from the Orbiting Astronomical Observatory (OAO-2). NASA SP-310. 1972.

Wormhoudt, J. and Lyons, R.B. IR/UV Tactical Missile Plume Signature Data Analysis: Vol 1. Contract F04611-79-C-0048. Aerodyne Research Inc., Bedford Mass., October 1981. (AD-C027 389 Secret Report)

VITA

Captain Stuart D. Williams [redacted] In 1959, he moved to Las Cruces, New Mexico where he graduated from High School in 1973. He attended the USAF Academy from which he received a Bachelor of Science Degree in Computer Science. Following graduation from pilot training in 1978, he remained at Reese AFB, Texas as a flight instructor in the 54th Flying Training Squadron. In 1981, he attended RF-4 upgrade training at Shaw AFB, SC and subsequently was assigned to the 38th Tactical Reconnaissance Squadron, Zweibrucken AB, Germany in 1982. In Germany, he served as a RF-4 flight instructor and flight examiner until entering the School of Engineering, Air Force Institute of Technology, in June 1985.

[redacted]

UNCLASSIFIED
SECURITY CLASSIFICATION OF THIS PAGE

REPORT DOCUMENTATION PAGE

Form Approved
OMB No. 0704-0188

1a. REPORT SECURITY CLASSIFICATION UNCLASSIFIED	1b. RESTRICTIVE MARKINGS
2a. SECURITY CLASSIFICATION AUTHORITY	3. DISTRIBUTION/AVAILABILITY OF REPORT Approved for public release; distribution unlimited
2b. DECLASSIFICATION/DOWNGRADING SCHEDULE	
4. PERFORMING ORGANIZATION REPORT NUMBER(S) AFIT/GSO/ENP/86D-3	5. MONITORING ORGANIZATION REPORT NUMBER(S)
6a. NAME OF PERFORMING ORGANIZATION School of Engineering 6b. OFFICE SYMBOL (If applicable) AFIT/ENG	7a. NAME OF MONITORING ORGANIZATION
6c. ADDRESS (City, State, and ZIP Code) Air Force Institute of Technonlogy Wright-Patterson AFB, Ohio 45433	7b. ADDRESS (City, State, and ZIP Code)
8a. NAME OF FUNDING/SPONSORING ORGANIZATION AF Wright Aeronautical Lab 8b. OFFICE SYMBOL (If applicable) AFWAL/AARI	9. PROCUREMENT INSTRUMENT IDENTIFICATION NUMBER
8c. ADDRESS (City, State, and ZIP Code) Wright-Patterson AFB, Ohio 45433	10. SOURCE OF FUNDING NUMBERS PROGRAM ELEMENT NO. / PROJECT NO. / TASK NO / WORK UNIT ACCESSION NO.
11. TITLE (Include Security Classification) See Box 19	
12. PERSONAL AUTHOR(S) Stuart D. Williams, B.S., Captain, USAF	
13a. TYPE OF REPORT MS Thesis 13b. TIME COVERED FROM _____ TO _____ 14. DATE OF REPORT (Year, Month, Day) 1986 December 15. PAGE COUNT 113	
16. SUPPLEMENTARY NOTATION	

17. COSATI CODES			18. SUBJECT TERMS (Continue on reverse if necessary and identify by block number)
FIELD	GROUP	SUB-GROUP	
17	05		Ultraviolet, Remote Sensing, Missile Detection

19. ABSTRACT (Continue on reverse if necessary and identify by block number)

Title: A PRELIMINARY STUDY ON THE USE OF THE ULTRAVIOLET EXHAUST PLUMES OF ICBMS FOR LAUNCH DETECTION

Thesis Chairman: James J. Lange, Major, USAF
Adjunct Professor of Physics

20. DISTRIBUTION/AVAILABILITY OF ABSTRACT ☑ UNCLASSIFIED/UNLIMITED ☐ SAME AS RPT. ☐ DTIC USERS	21. ABSTRACT SECURITY CLASSIFICATION UNCLASSIFIED
22a. NAME OF RESPONSIBLE INDIVIDUAL James J. Lange, Major, USAF	22b. TELEPHONE (Include Area Code) 513-255-6144 22c. OFFICE SYMBOL AFWAL/AARI

DD Form 1473, JUN 86 *Previous editions are obsolete.*

SECURITY CLASSIFICATION OF THIS PAGE
UNCLASSIFIED

The purpose of this investigation was to conduct preliminary research into the use of the ultraviolet plumes of ICBMs for launch detection. The thrust of this research was in an effort to exploit the middle UV (200-300 nm) for launch detection and possible tracking. Specifically, this thesis reviewed the current open literature on the UV signatures of ICBMs, current ultraviolet background data, the state of UV detector technology, and simple sensor design considerations. From these investigations a baseline sensor system was assumed which was compatible with existing technology.

Using the baseline sensor system, representative target intensities and background radiances, first order signal-to-noise calculations were performed. The results of these calculations revealed that the current state of UV detector technology and the magnitude of representative plume intensities are sufficient to allow for ICBM detection from a geosynchronous sensor system. However, because of the UV target signal absorption by the ozone layer, adequate SNR can not be maintained below approximately 40-50 km. These results indicate that further study into this problem is warranted and several recommendations are included for consideration.